

## **RF Coil Technology for Small-Animal MRI**

F. David Doty, George Entzminger, Jatin Kulkarni, Kranti Pamarthy, and John P. Staab

### **Abstract**

A review of the theory, technology, and practice of RF coils for small-animal MRI is presented that includes a brief overview of MR S/N analysis and discussions of the various coils commonly used in small-animal MR – surface coils, linear volume coils, birdcages, and their derivatives. The scope is limited to mid-range coils – coils where the product ( $fd$ ) of the frequency  $f$  and the coil diameter  $d$  is in the range of 2-30 MHz-m. Common applications include mouse brain and body coils from 125 MHz to 750 MHz, rat body coils up to 500 MHz, and small surface coils at all fields. In this regime, all the sources of loss (coil, capacitor, sample, shield, and transmission lines) are important. All such losses may be accurately captured in some modern full-wave 3D EM software, and new simulation results are presented for a selection of surface coils using Microwave Studio (MWS) 2006 by Computer Simulation Technology (CST), showing the dramatic importance of the “lift-off effect”. Standard linear circuit simulators have been shown to be useful in optimization of complex coil tuning and matching circuits. There appears to be considerable potential for trading S/N for speed using phased arrays, especially for a larger field of view. Circuit simulators are shown to be useful for optimal mismatching of ultra-low-noise preamps based on the E-PHEMT (Enhancement mode Pseudomorphic High Electron Mobility Transistor) for optimal coil decoupling in phased arrays. Cryogenically cooled rf coils are shown to offer considerable opportunity for future gains in S/N in smaller samples.

## RF Coil Technology for Small-Animal MRI

F. David Doty, George Entzminger, Jatin Kulkarni, Kranti Pamarthy, and John P. Staab

**Introduction.** The RF coil is recognized as being of critical importance for obtaining maximum S/N in MRI, so naturally many papers have appeared on this subject. However, the vast majority of MRI RF coil articles over the past two decades have focused on large coils, where sample losses strongly dominate, or on microcoils, where sample and capacitor losses are negligible. Fewer have addressed the mid-range coils, seen in the majority of small-animal applications, where all the sources of loss (coil, capacitor, sample, shield, and transmission lines) are important. The human MRI market is more than an order of magnitude larger than the small-animal (or pre-clinical) MRI market, so it is not surprising that advanced and generally sufficient software tools have been available commercially from several vendors for at least five years for applications where coil losses are not too important, while the available options are still not always fully satisfactory for mid-range coils.

Another distinction between many clinical MR volume coils and those for small-animal research is that the former are often intended for a rather narrow range of loadings, while the latter are often desired to operate as optimally as practical from the nearly unloaded condition to the case of being stuffed to the limit. This, along with the higher operational frequencies, makes tunability more of an issue. Often the tuning/matching circuitry must be somewhat remote from the coil, and this makes optimization complex.

The focus of this (somewhat pedagogical) technology review is on mid-range coils – coils where the product ( $fd$ ) of the frequency  $f$  and the coil diameter  $d$  is generally in the range of 2-30 MHz-m. This would include, for example, mouse brain and body coils from 125 MHz to 750 MHz, rat body coils up to 500 MHz, and small surface coils at all fields. Coils in this range, except near the upper end, are often perceived by research managers to be relatively simple to optimize and build. Hence, many MR research programs have electronics and machine shop facilities devoted to building such coils.

We begin by presenting a brief overview of MR S/N analysis, followed by brief discussions of the various coils commonly used in small-animal MR (surface coils, linear volume coils, birdcages). We include some new simulation results on surface coil optimization and show the importance of the often overlooked “lift-off effect”. Finally, we briefly discuss advanced PHEMT pre-amps and mismatching requirements for phased arrays from a numerical circuit simulation approach and potential future progress from the use of cryogenically cooled rf coils.

**S/N in Complex Coil Circuits.** The dependence of the S/N following a single  $90^\circ$  pulse when all the resistive losses (coil, capacitors, sample) are at the same temperature  $T_n$  may be expressed in a number of ways. We have found the following often most useful in coil design [1, 2]:

$$S/N = \left[ \frac{\hbar^2 \sqrt{2\pi\mu_0}}{12k_B^{3/2}} \right] \left[ \frac{n_s \gamma I_x (I_x + 1) \sqrt{T_2^*}}{T_s \sqrt{T_n + T_p}} \right] (\eta_E \eta_f Q_L V_S)^{1/2} \omega^{3/2} \quad (1)$$

where  $\hbar$  is Plank's constant divided by  $2\pi$ ,  $\mu_0$  is the permeability of free space,  $k_B$  is Boltzmann's constant,  $n_s$  is the number of spins at resonance per unit volume,  $\gamma$  is the magnetogyric ratio,  $I_x$  is the spin quantum number,  $T_2^*$  is the effective spin-spin relaxation time,  $T_s$  is the sample temperature,  $T_n$  is the probe noise temperature,  $T_p$  is the effective preamp noise temperature,  $\eta_E$  is the rf efficiency (the fraction of power dissipated in the sample coil),  $\eta_f$  is the magnetic filling factor of the sample coil,  $Q_L$  is the matched, loaded, circuit quality factor,  $V_S$  is the sample volume, and  $\omega$  is the Larmor precession frequency,  $\gamma B_0$ .

The primary problem with Eq. 1 is that it has not been easy to calculate magnetic filling factor with good accuracy except for very simple cases until rather recently. Filling factor is traditionally defined as the magnetic energy in the transverse component of the magnetic field throughout the sample divided by the total magnetic energy  $U$  throughout all space (recall  $U = I^2 L/2$  for a simple coil). However, in order for the concept to apply properly to circular polarization (**CP**), it is better to define  $\eta_f$  in terms of the *transverse rotating* field component  $B_1$ :

$$\eta_F = \frac{\int_S B_1^2 dV_S}{\mu_0 U}. \quad (2)$$

If we assume  $T_p$  is negligible compared to  $T_n$  (a reasonable assumption with state-of-the-art tuned preamps, except perhaps for phased arrays and cryoprobes, as we will see later) and losses are confined to a single resistor  $R_0$  of temperature  $T_n$  in series with a lossless sample coil and capacitor, then for given MR test conditions (sample,  $B_0$ ,  $T_2^*$ ,  $T_S$ , and method), the following equation can be derived, either from Eq. (1) or from the principle of reciprocity [2-6]:

$$S/N \propto \frac{B_1 V_S}{i \sqrt{R_0 T_n}}, \quad (3)$$

where  $i$  is the sample coil current and  $B_1$  is the mean rf CP field generated within the sample by current  $i$ . Since the Johnson noise voltage is proportional to  $(R_0 T_n \delta f)^{1/2}$ , the signal voltage, from Eq. (3), is proportional to  $B_1 V_S / i$ . This expression for signal voltage is valid irrespective of the noise source temperature [5], but it is often not particularly convenient. Equation (3) is easily cast into the following form, which is more useful in practical probe design and evaluation, where power is dissipated in numerous losses of uniform temperature  $T_n$  in a complex circuit:

$$S/N \propto \frac{B_1 V_S}{\sqrt{P_T T_n}}, \quad (4)$$

where  $P_T$  is the total transmitter power required to generate  $B_1$  (power applied at the disconnected preamp port, so that transmission line losses are properly included). Both Eqs. (3) and (4), usually without the  $T_n$  in the denominator, are commonly referred to as statements of the principle of reciprocity. (Note that for linear polarization,  $B_1$  is half the peak rf field strength. Also, the  $B_1$  field strength is often expressed as the reciprocal of the pw90, the time required to rotate the magnetization  $90^\circ$ .) However, the above expressions fail when the various losses are at significantly different temperatures. Clearly, one cannot ignore the  $T_n$  factors in cryo-probes, which are now in widespread usage for liquids NMR and appear to be coming soon for solids NMR and micro-imaging.

Equation (4) is easily extended, in a more generalized statement of the principle of reciprocity, to handle complex circuits where various losses are at different temperatures as follows [7]:

$$S/N \propto \frac{B_1 V_S}{\sqrt{\sum P_n T_n}}, \quad (5)$$

where  $P_n$  is the transmit power dissipated in the nth resistance of temperature  $T_n$  when generating  $B_1$ , and the summation is over all resistances (sample, coils, capacitors, shields, and transmission lines) in the circuit. One way to show this is to transform each loss into an equivalent resistor  $R_n$  in series with the sample coil [7]. In large coils at high fields, the denominator summation is dominated by the power dissipated in the sample, which is usually at 310 K for *in vivo* applications. Since sample loss is proportional to the integral of  $\sigma E^2$  over the full sample, where  $\sigma$  is the sample conductivity and  $E$  is the electric field, optimization of coils for these cases boils down to minimization of the integral of  $E/B_1$ .

In most mid-range coils, losses in the sample coil, capacitors [4], and transmission lines are also significant, and the complete circuit must be optimized. Equation (5) may be cast into the following form, which is generally more easily related to the results from linear circuit simulation software in the analysis of complex circuits:

$$S/N \propto \frac{v_c V_S}{\sqrt{L_C V_C \sum P_n T_n}}, \quad (6)$$

where  $L_C$  is the sample coil inductance,  $V_C$  is the coil volume, and  $v_c$  is the *voltage* generated across the sample coil when pulse power  $P_T$  is applied at the impedance-matched port. The  $L_C$  in the denominator may be initially surprising. However, the derivation of the above is straightforward for a specific sample-coil type, and it has been experimentally validated in numerous experiments [7]. Eq. (6) shows that the relative S/N (for a given sample coil,  $T_2^*$ , etc.) in a complex circuit (containing various coils, capacitors, and transmission lines between matching elements, sample coil, T/R switch, and preamp) is indicated simply by the voltage induced at the sample coil by a given power applied at the disconnected preamp input port.

Thus, the rf “coil” optimization problem consists of two major parts: (1) minimization of the integral of  $E/B_1$  for the sample coil (where the numerator is integrated over the full sample, and the denominator is integrated only over the homogeneous field region), and (2) maximizing the efficiency of delivering rf power to the coil when viewed from the transmit perspective – even if the coil is for receive only. The first task can only be fully addressed using full-wave software with effective algorithms for handling conductor surface losses, even though perturbation methods permit accurate workbench measurement of the magnetic filling factor [4] and  $Q_L$  may be easily measured. The second task is best addressed using common linear circuit simulators, such as ARRL Radio Designer, SPICE, Ansoft Designer, or GENESYS. While the simplified analytical approaches usually presented in the professional literature are useful in providing insights, we find the numerical tools to be superior in practice – a point we will emphasize.

It is necessary to keep in mind several assumptions in the above analyses: (1) the preamp’s noise temperature is low compared to that of the coil circuit; (2)  $T_2^*$  is not adversely affected by coil magnetism – an issue that is generally of no consequence in design of coils larger than 80 mm but often becomes of critical importance for coils smaller than 12 mm; and (3) the frequency-domain filter bandwidth is equal to  $1/(\pi T_2^*)$ . Note that this noise bandwidth may be established by exponential multiplication of the signal acquisition prior to the Fourier Transform (FT) or by signal processing (such as line broadening) after the FT.

**Full-wave 3D EM Software.** It appears that most 3D software validations on MRI coils have not confirmed the accuracy of the software for complex, mid-range coils where all types of losses are significant. In mid 2002, we carried out rather detailed evaluations of three leading “full-wave 3D EM” packages and concluded that for most mid-range NMR and MRI rf coil problems, Microwave Studio (MWS) 4.3 by Computer Simulation Technology (CST) was better suited and more accurate than the other software we evaluated (HFSS by Ansoft, and XFDTD by REMCOM) [8]. Others have more recently shown that Ansoft HFSS also gives accurate results for some aspects of small-coil problems [9].

The CST software is based on a discretized solution of the integral formulation of Maxwell’s equations; hence, the method is referred to as Finite Integration Technique (FIT) [10]. To solve these equations, a calculation domain is defined enclosing the application problem. An important part of obtaining accurate solutions with reasonable mesh sizes lies in the detailed handling of mesh elements containing several different materials, especially when one material is a lossy metal and another material is a dielectric. CST has put considerable effort into optimizing the calculation of the mean effective fields and losses within these troublesome cells that generally cover most of the surfaces of conductors in complex structures or may even be divided by several thin sheets of conductors.

The discretized mesh equations can be solved either in the time domain by a transient Finite Difference Time Domain (FDTD) approach or in the frequency domain using second-order harmonic relations. Until quite recently, we have usually used the transient method, primarily because it provides a broad spectrum solution but also because the frequency domain solver was not well developed until late in 2006. We observe that the CST time-domain solver usually gets the rf copper losses right within ~10% (the typical limit of our experimental accuracy) for thick conductors and wires, and also for foil conductors when the current densities are not too different on opposite sides of the foil. However, where current densities are radically different on opposite sides of foils, as frequently arises in birdcages for example, it has often underestimated copper losses significantly. Recent tests of the frequency-domain solver with tetrahedral meshing indicate it is both faster and more accurate for high-Q coil problems. The eigenmode solver is several orders of magnitude faster than the other solvers, but it does not handle lumped elements nor does it handle losses well.

In all our simulations, the tuned coil is excited with a broadband 50  $\Omega$  pulse source of Gaussian distribution, 14.14 V peak, centered very near resonance, which delivers 0.5 W to the coil when matched to 50  $\Omega$ . Also, the simulation space (which includes the coil, sample, and shield) has copper boundaries. The mode frequencies are usually calculated within 2% of the experimental values (even for double resonance coils), and the calculated  $B_1$  magnitude often agrees within 5% with the MR experiment. While the  $B_1$  magnitude can sometimes be off by up to 25%, the  $E/B_1$  integral is probably generally accurate within a few percent.

**Surface Coils.** The surface coil is widely used in MRI, as it is often a convenient and effective way of obtaining higher localized S/N than can be obtained with volume coils, but it is important to appreciate that the advantages in small-animal applications are often not as great as is seen in human applications, where the volume coil is almost always sample-noise dominated. Several excellent review articles have appeared

[11-13], along with many other articles [14-22], several book chapters [23, 24], and an elementary book devoted to the subject of mid-sized MRI coils [25]. We will not attempt to repeat here much of what is already quite accessible. Rather, our emphasis will be on some implementation and optimization details that are less well covered in the literature.

Surface coils become advantageous for MR when sample losses are dominant and/or the region of interest is very near the surface. A 12 mm surface coil, for example, will be superior to a well optimized (short) birdcage of 20 mm diameter for  $^1\text{H}$  mouse brain MRS at 7 T only for features within 6 mm of the surface. At greater depths, the small birdcage has higher S/N in addition to its strong advantage in rf homogeneity. Here, *coil* (not sample) losses are dominant for both the surface coil and the birdcage, but the surface coil achieves higher S/N over a small region near the surface because of its higher filling factor.

One usually prefers to use the surface coil as receive-only if possible, as more efficient pulse-sequence options are available with the uniform excitation field of a body transmit coil. However, there are times where there is no space for a suitable body coil, or perhaps it is preferable to restrict the transmit region to the receive region for SAR reasons, as in double-resonance cross-polarization or high-power  $^1\text{H}$  decoupling. For these cases, the Transmit/Receive (T/R) surface coil is appropriate.

For surface coils smaller than  $\sim 50$  mm, it is important that their capacitors have low magnetism. In most cases, it is sufficient to simply specify that the standard nickel barrier in the capacitor terminations be omitted, but with very small coils it may be necessary to be even more discriminating. We recently measured the mean bulk susceptibility  $\chi$  of a number of “non-magnetic” (nickel-free) chip capacitors. The susceptibilities of the TEMAX series CHB capacitors were in the range of -4 to 0 ppm (E-6 SI volumetric units), while susceptibilities of the ATC700B series were in the range of 15 to 30 ppm, the Cornell Dublier MCM series were in the 30 to 50 ppm range, and the ATC100B capacitors were in the range of 5 to 10 ppm.

**Detailed RF Circuit Modeling.** **Figure 1** depicts a useful circuit model, with node reference numbers, for a commonly used T/R surface coil with remote tune/match, and a photo of a typical coil is shown in **Figure 2**. The sample coil  $L_S$  is shown with a node explicitly at its center so the voltage at this point is directly available to confirm that the coil is balanced. To reduce the clutter, stray capacitances are not shown explicitly, but they are always included appropriately in the model. The sample losses appear in the Q of  $L_S$ . For a 12 mm 300 MHz unsegmented coil, for example, a typical value ( $X_L/R_S$ ) might be 240 unloaded and 100-180 loaded. (Remember that the matched  $Q_L$  of a circuit is half the unmatched  $Q_0$  of a tank circuit, and the unmatched  $Q_0$  of a tank circuit would be half that of the coil and the capacitor separately if, for example, their  $Q$ s were equal.) As shown in Eq. (6), the object of the circuit optimization is to achieve the highest possible voltage across the sample coil (nodes 12, 13) when excited with a given power at the 50- $\Omega$  port labeled RF.

All the elements are modeled with realistic Q values and lead inductances. The matching and balancing is most conveniently done capacitively, so the majority, but not all, of the coil tuning capacitance,  $CC$ , is placed directly across the sample coil with minimal lead length. A reasonable estimate of the quality factor  $Q_C$  of a low-loss ceramic capacitor of capacitance  $C_p$  picofarads at  $f_0$  MHz is given by the following:

$$Q_C \approx 1.5E07 C_p^{-0.85} f_0^{-1.35} \quad (7)$$

(For example, a hi-Q 10 pF chip may have  $Q_C$  of  $\sim 450$  at 500 MHz. The  $Q$ s of the zero-temperature-coefficient types, such as ATC700B, are  $\sim 20\%$  lower.) The small tuning variable  $CT1$  may need to be nearly a centimeter away to prevent shimming difficulties, in which case the leads between it and  $CC$  may need to

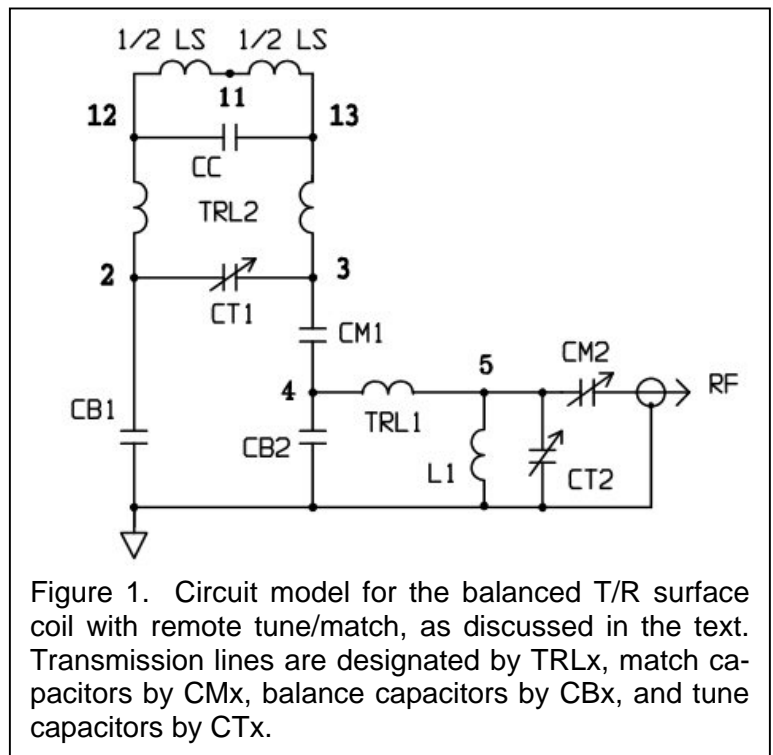


Figure 1. Circuit model for the balanced T/R surface coil with remote tune/match, as discussed in the text. Transmission lines are designated by  $TRL_x$ , match capacitors by  $CM_x$ , balance capacitors by  $CB_x$ , and tune capacitors by  $CT_x$ .

be accounted for. They are shown here as transmission line TRL2, which, for example, may be a balanced 100  $\Omega$  line, 8 mm long.

In the older circuit simulators, the input consisted of a “node list” – a list of the circuit elements with the node numbers to which they were connected, along with additional parameters giving relevant characteristics, such as propagation velocity, length, Q, etc. In the more recent simulators, the input is simply the circuit schematic, such as Figure 1, with descriptions of each of its elements.

While most clinical coils are not user tunable, it is generally useful to have some remote tune/match adjustment capability in small-animal applications, as the frequency of the surface coil can be shifted significantly by changes in its location relative to the transmit coil, sample, or shield. Sufficient remote tunability may be achieved without significant loss in S/N if the VSWR (Voltage Standing Wave Ratio) on the cable to the surface coil (transmission line TRL1) between the surface coil and the remote tune network is kept moderately low. A coil L1 in parallel with remote tune variable CT2 tuning out about half of the maximum value of CT2 allows a plus or minus reactance adjustment and often doubles the tuning range for a given loss in efficiency. Keeping the length of TRL1 roughly equal to  $n\lambda/2$  is also often helpful, though not essential. The effect of the loss in TRL1 on S/N is readily seen by changing its attenuation coefficient in the simulation from the actual value (for example, 0.145 dB/m for Belden 1855 at 200 MHz) to zero and noting the increase in the voltage across the sample coil. (It is not straightforward to get the voltage data at nodes that are not ports in some simulators, such as GENESYS, but there are usually work-arounds. For example, very high impedance ports, having negligible load on the circuit, can be defined at internal circuit nodes where the voltage data are needed.) Likewise, the effects of the losses in all the capacitors and L1 are readily determined by changing their Qs from actual values to infinite and noting the change in the voltage across the sample coil. With a little experience, one can fairly quickly come up with appropriate values for all the components that achieve the desired objectives: tuned to the desired frequency, nearly zero voltage at the center of the sample coil, total S/N loss from all components other than the sample plus the coil itself less than 10% (half of which will probably be in CC and perhaps a third in TRL1), no parasitic mode nearby, and adequate tune and match adjustability with CT2 and CM2.

It should be emphasized that improper choice of matching capacitor CM1 could result in half the S/N being lost in TRL1, even with the coil balanced and the circuit tuned and matched to 50  $\Omega$  by CM2. This problem is often exacerbated



Figure 2. A 20 mm balanced T/R surface coil with heavy, magnetically compensated, parallel conductors. The thin acrylic coating over all the parts is not obvious, and the remote tune/match network, included in Figure 1, is not shown here but is at the remote end of the feed cable.

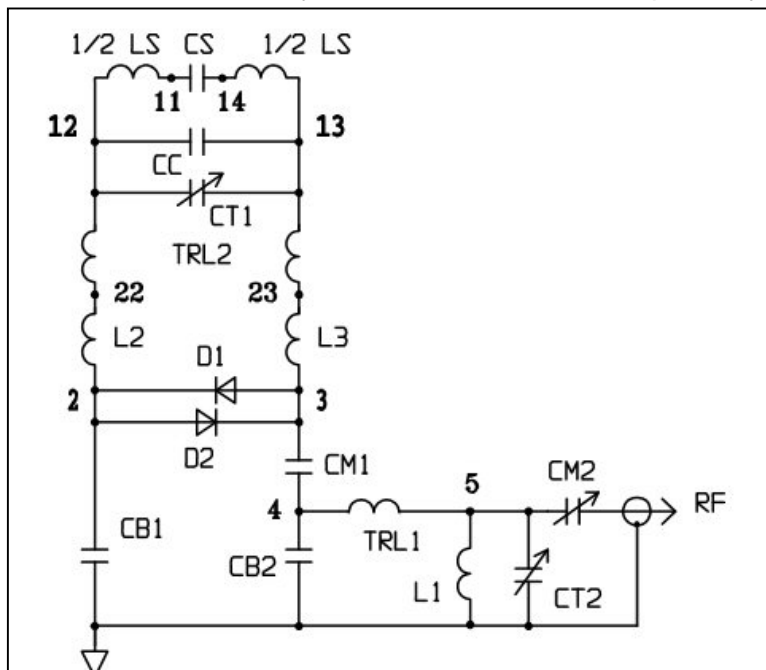


Figure 3. Circuit model for the capacitively segmented, passively detuned surface coil with remote tune/match.

by the use of a rather light-weight rf line for improved flexibility (such as RG174, 0.32 dB/m at 200 MHz) for perhaps the first 15 cm connected to the coil. Note that lower losses for a given rf line diameter will usually be seen if TRL1 is a 75  $\Omega$  line, such as Belden 1855, even though the rf preamp is usually optimized for a 50  $\Omega$  source.

A common mode (with nearly zero efficiency) will always be present, and often it will initially be not too far from the desired differential mode. Its location will usually be fairly well predicted if the stray capacitances in the coil model (from nodes 11, 12, and 13 to ground) are correct (often about 2 pF at node 11 for a 2 cm coil). Its position is dependent on just about everything except CC and CT1, so it can usually be moved well away from the efficient mode without too much difficulty. These complications emphasize the need for the kind of detailed circuit analysis that is best handled with standard circuit simulators rather than analytical closed-form solutions, which usually include unrealistic simplifications. However, there are limitations in this model, primarily because there is no attempt to include electric couplings to the body transmit coil. As a result, common mode problems may still arise that may be able to be addressed with cable traps [18] – a subject we return to later.

We avoid using coupling loops (in place of capacitive balancing) because they are much more difficult to model accurately, are less convenient with active decoupling, and usually offer no advantages. We also do not find it beneficial to use a balanced pair of lines for TRL1, as has been recommended in the literature.

**Surface Coil Decoupling.** While the use of separate transmit and receive coils permits uniform excitation with better local S/N, the interactions between the coils often leads to problems. If the receive coil is not “decoupled” during the transmit pulse, its resonance dominates and destroys the homogeneity of the transmit field [15]. (Note the distinctly different meaning here for “decoupled” than its more common meaning in double-resonance NMR spectroscopy.) With a linear transmit coil, the coils may sometimes be adequately decoupled by orienting the surface coil so that its  $B_1$  is orthogonal to that of the transmit coil. Another approach that often works well (when there is adequate space) is the self-shielded surface coil, also called a gradiometer or quadrupolar coil [22], consisting of two loops, one above the other, with oppositely directed currents. Such a coil also has a reduced depth of field, which is often a disadvantage, but it can have higher S/N because of reduced far-field losses when used on large samples [22]. However, the most commonly used method of coil decoupling is detuning – either passively or actively.

**Figure 3** illustrates an effective approach for passive detuning in small coils at high frequencies [15, 20]. The switching (PN) diodes D1 and D2 (we’ve recently used Vishay type BAS16D, which have sufficiently low magnetism) look like small capacitors ( $\sim 1$  pF each) during receive and like shorts ( $\sim 1$   $\Omega$ ) during an intense transmit pulse. The small coils (L2, L3) and very short (4-10 mm) transmission line (TRL2) between the diodes and CC are resonant with CC plus CT1 when the diodes are shorted. Thus, there is a high impedance at the ends of the surface coil LS (nodes 12, 13) in the absence of the sample coil, and current in LS is minimized during transmit – as desired to minimize its effect on the transmit field. One can sometimes dispense with L2 and L3 and have adequate decoupling with the diodes placed directly across CC, but usually this approach is not as satisfactory [15].

Figure 3 further illustrates the need for good models and accurate circuit simulations. Efficiency of this circuit is seen to suffer badly if L2 and L3 are not small compared to LS or if CC+CT1 is not large compared to CB1 and CM1. Because of the rather large off-state capacitance in the diodes and other parasitics (again, not shown), efficient conditions cannot be achieved above  $\sim 200$  MHz with a surface coil larger than  $\sim 20$  mm ( $\sim 20$  nH) unless it is capacitively segmented – i.e., a capacitor (CS) must be inserted opposite CC to negate about half of LS. For the T/R coil of Figs. 1 and 2, one can go to considerably higher inductance and

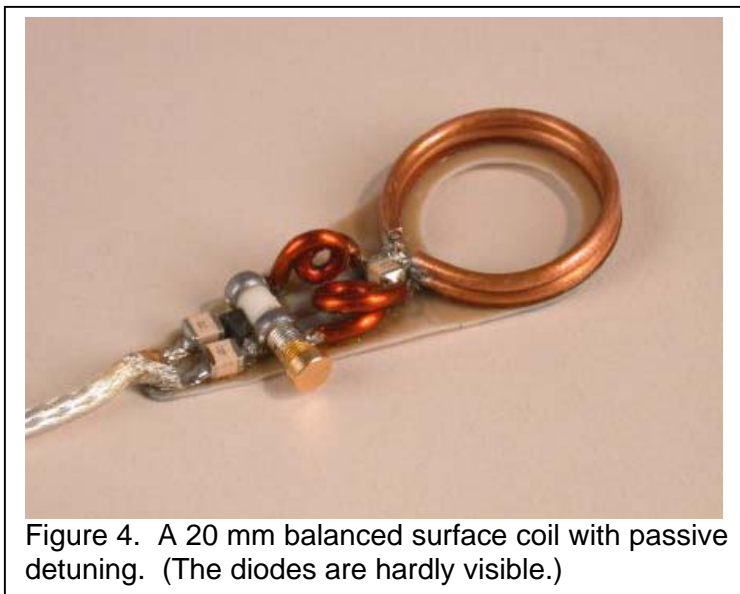


Figure 4. A 20 mm balanced surface coil with passive detuning. (The diodes are hardly visible.)

frequency before CS is required. However, the segmenting capacitor may be desired for reducing dielectric losses in the sample for  $fd$  greater than  $\sim 5$  MHz-m, as will be shown in the next section. When optimally implemented, this passive detuning circuit, shown also in **Figure 4**, typically degrades coil S/N by  $\sim 5\%$ .

It was noted earlier that the switching diodes in Figure 3 look like shorts during an *intense* transmit pulse. However, the transmit field may not have sufficient intensity during its full duration for sufficient detuning using the passive method of Figure 3, so active detuning may be required. Active detuning is also useful in some  $B_1$  field mapping techniques.

An active detuning circuit is shown in **Figure 5** in which the sample coil is segmented. A single PIN diode D1 (such as type MA4P505-1072, 500 V, 0.7 pF,  $1 \Omega$  at 10 mA, 1.5 W, 2  $\mu$ s minority carrier lifetime) may be used. Inductors LB1, LM1, and LM2 are used in balancing and matching so that a “DC” path is provided for biasing the diode using a “DC” detune current pulse superimposed on the rf line. Other components, as in Fig. 3, may again be useful in reducing losses in TRL1 or moving a common mode.

As with the passively detuned circuit, CC must be large compared to the off-state capacitance of D1 plus parasitics. Also, the magnitude of the reactance of CC should be small compared to the magnitude of the reactances of LB1, LM1, and LM2, all of which, of course, must be air core, as they must be non-magnetic and be predictable in the magnetic field  $B_0$ . Optimization using a circuit simulator is still straightforward: simply set the losses in any component to zero and note the increase in the voltage across the sample coil to see how much the S/N is being degraded by that component. With a little care, total S/N loss from all tuning components can be under 15% even for the small coil.

While we have discussed ways to deal with the magnetic interactions of the transmit coil with the surface coil, we have thus far looked at the surface coil circuit models only in isolation from the transmit coil. Care is always taken to minimize and balance the electric fields from the transmit coil, but these electric fields and their standing waves in the sample still often have significant interactions with the surface coil and its cable. These interactions produce voltage and current signals on the shield of the surface coil cable that would not be captured in the above circuit models, which assume the shield of this cable is everywhere at ground potential. The common-mode shield current and voltage distributions may be similar to what is seen on dipole antennas [18], characterized by the free-space wavelength. One approach to suppressing shield currents is to insert one or more cable traps [18], where the object is to insert a higher impedance to common-mode cable signals with little effect on differential-mode signals. Cable traps may also be a method of dealing with common-mode resonances that are captured in the circuit models presented earlier, though we find the circuit optimization methods described earlier more effective.

One method of making a cable trap has been coiling a short portion of the rf cable (TRL1) into one or two small turns (depending on the frequency), exposing the shield at the ends of this coil, and placing a capacitor across it that tunes it to the resonant frequency of the surface coil. An approach that has several distinct advantages is to place a coaxial resonator, tuned to the frequency to be suppressed, around the cable [26]. This is essentially a compact, lumped-element version of the (cumbersome) tri-axial “bazooka” [27]. An adjustable, split version of the coaxial resonator has been patented by IGC Medical Advances [28].

**Surface Coil Optimization.** For coil  $fd$  below  $\sim 4$  MHz-m (e.g., a 14 mm coil at 300 MHz), coil resistance losses are often dominant, so minimization of these losses by the use of very heavy conductors is clearly beneficial. For example, two magnetically compensated (copper-clad aluminum) parallel wires (of 1.6 mm diameter), as shown in earlier figures, was found to give  $\sim 30\%$  higher S/N than a single 1 mm wire for a 20 mm 128 MHz coil. Here, the benefit was little more than half due to increase in  $Q_L$ . The increase in

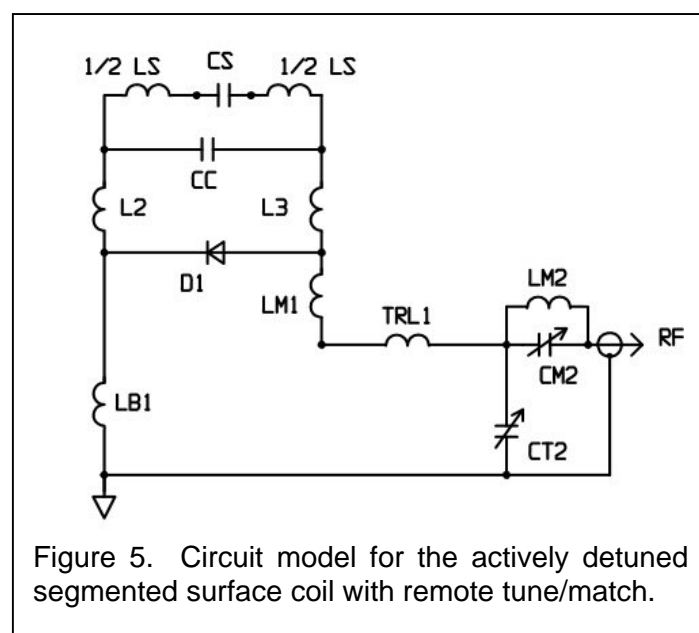


Figure 5. Circuit model for the actively detuned segmented surface coil with remote tune/match.

magnetic filling factor  $\eta_F$  from the reduction in the intense  $B_1$  near the conductor surface was nearly as significant. To understand how this can be consistent with Eq. 3, as it is clear that the ratio  $B/i$  is not improved (actually, slightly degraded) by the addition of the second parallel wire, one must recognize that the reduction in  $R$  is considerably greater than simply inverse with  $Q$ , as the inductance is also reduced by the addition of the parallel wire, and  $R=L/Q$ . (The point here is that Eqs. 1 through 6 all provide useful and valid insights.) Of course, for larger  $fd$ , the reduction in coil resistance becomes less important, but the reduced inductance of the heavy coil continues to be beneficial, as it reduces near-field  $E/B_1$  within the sample and thus reduces sample losses.

A portion of the  $\mathbf{E}$  field within the sample, the so-called “conservative  $\mathbf{E}$  field” (because it arises from the scalar potential, rather than from  $d\mathbf{B}/dt$ ), may be decreased by reducing the coil’s inductance. Hence, multi-turn coils are almost never optimal for  $fd$  above 2 MHz-m. Capacitive segmentation allows one to reduce the effective inductance of a conductor element and thus *sometimes* reduce the losses from the conservative  $\mathbf{E}$  field. However, the series resistance of the capacitor is always greater than that of a piece of copper of similar size, and the concentrated  $\mathbf{E}$  fields very near the capacitors may increase total sample losses. Accurate simulations or experiments are generally required to determine the optimum.

**Table 1** presents some results from a number of simulations, using CST MWS 2006, of 16 mm coils at different frequencies, with two different loadings, varying segmentation, and several different air gaps between the coil and sample. In all cases, there were two parallel 1.6 mm wires as shown in Figure 6. The “light load” is a sphere of 30 mM saline, 20 mm in diameter (4.2 g), with center ~9 mm from the central plane of the 2-wire surface coil, as shown in **Figure 6**. The “moderate load” is a sphere of 50 mM saline, 40 mm in diameter (33 g), with center ~20 mm from the plane of the coil. The light load is somewhere between the loading of a

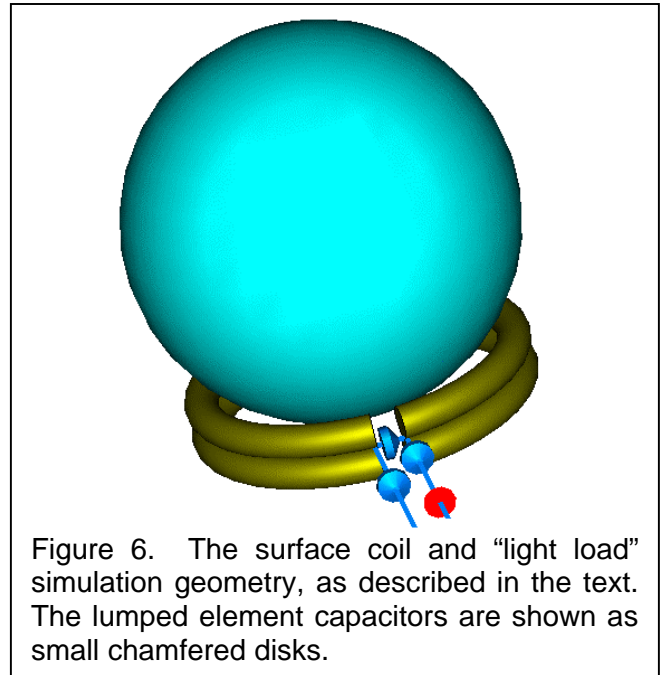


Figure 6. The surface coil and “light load” simulation geometry, as described in the text. The lumped element capacitors are shown as small chamfered disks.

Table 1. Segmentation, Spacing, and Loading of a 16 mm Surface Coil								
f MHz	# coil segments	C pF	$Q_C$	Load	Air Gap mm	$Q_L$	Sample losses, %	H, A/m, @ 0.5 W
200	1	31	550	light	0.6	148	22	69
200	2	62	300	light	0.6	81	32	51
200	2	61	310	mod.	1.6	93	20	60
300	1	13.5	640	light	0.6	132	35	59
300	2	27	360	light	0.6	78	48	42
300	2	28	350	light	1.6	118	14	53
300	2	26.5	360	mod.	1.6	105	31	50
500	1	4.5	820	light	0.6	119	55	47
500	2	9.5	440	light	0.6	105	39	42
500	3	14	310	light	0.6	86	30	38
500	2	9.8	420	light	1.6	131	26	46
500	1	4.4	820	mod.	1.6	93	66	44
500	2	9.2	450	mod.	1.6	76	54	40
750	2	4	530	light	0.6	93	57	38
750	2	4.1	530	light	1.6	119	43	42
750	2	4.2	530	light	2.0	132	38	43
750	3	6.1	370	light	1.6	100	34	38

mouse head and a rat head, and the moderate load is midway between the loading of a mouse and rat body. In all cases, (1) appropriate values are used for the capacitor resistances, (2) circuit losses external to the surface coil and its capacitors are ignored, (3) the coil and sample calculation space are enclosed in a large enough copper box to make boundary effects negligible, and (4) the transient solver was used with no symmetry planes and adequate mesh refinement in the vicinity of the coil. The  $H$  field magnitude ( $A/m$ ,  $2B_1/\mu_0$ ) at 0.5 W excitation (tuned, matched, and balanced) is given on the  $z$  axis, 8 mm from the center of the surface coil. Since all the losses are at the same temperature and all the coils are driven at 0.5 W, the S/N for a given voxel size is simply proportional to this calculated  $H$ . The calculated sample losses as a percent of total are also listed, which permits estimation of the unloaded matched  $Q$ ,  $Q_U$ . (Careful NMR and MRI experiments on a number of cases similar to those simulated here indicate the CST MWS 2006 software can generally be trusted to get the  $H$  field magnitude right within  $\sim 8\%$  and the homogeneous mode frequency within  $\sim 2\%$  for problems of this type.)

Note that performance is significantly degraded if the space between the sample and the coil is suboptimal – i.e., the “lift-off effect” [22]. In practice, coils in the 1-3 cm size range are often mounted on a teflon substrate with copper shielding patches between the capacitors from the sample. The higher dielectric constant of teflon (2.1) compared to air increases the spacing needed for optimum performance, but the floating shield patches may reduce the required space a little. These details were omitted to speed up the simulations without significantly altering the conclusions. Another difference between the simulated cases and the common practice is the solder joint connections, which may add about 15% to coil losses. Also, the coil is usually given a thin acrylic coating, which has negligible effect.

The results show there is often more to be gained from increased spacing from the sample than from increased capacitive segmentation. However, segmentation is often needed just to get a detuning circuit to work efficiently, as noted earlier. The simulations show it is very important to have the coil spaced away from the sample – a teflon foam substrate of thickness 5-10% of the coil's diameter is normally optimum for the T/R surface coil, but a larger separation may be useful in further minimizing electric field interactions that are more likely to be troublesome in receive-only applications. It has recently been again suggested that coaxial loops offer some S/N advantage [29, 30], but the arguments and data are not yet convincing.

Perhaps the most surprising result is that the most common coil-quality metric,  $Q_U/Q_L$ , is often misleading for surface coils (and, by analogy, for array coils). For example, this ratio is approximately 2 for the second 300 MHz coil listed in Table 1, while it is under 1.2 for the third 300 MHz coil, both of which are with the same load. Yet the second of these coils has 25% higher S/N, whereas estimation of relative merit of these coils simply by their  $Q_U/Q_L$  ratios would suggest the first has 30% higher S/N. This point can hardly be over emphasized. The  $Q_U/Q_L$  ratio is more often useful for homogeneous volume coils, but even there it also is often misleading, as we note later in comparing litz coils to birdcages.

The rf magnetic field from the loop surface coil over most of its effective region is normal to its plane. A pair of back-to-back D coils (also called a butterfly coil) can be used to generate an rf magnetic field just below their surface that is orthogonal to that of the loop surface coil and, for proper orientation of the D coils, is also orthogonal to  $B_0$  [19, 31]. Hence, the combination of the loop and pair of D coils, as shown in **Figure 7**, can be used for circular polarization, which may improve S/N in cases where sample losses are strongly dominant. However, when coil losses are dominant, S/N from the combination would usually be lower, as the coil interactions decrease both the unloaded  $Q$ s and the filling factors of both coils.

The loop/D combination is also often used for double resonance (e.g.,  $^1H/^{31}P$ , or  $^1H/^{19}F$ ). In many cases, it permits higher S/N at both frequencies than the alternative of double-tuning a single loop, though many methods to this latter approach have often been used [17]. Coplanar, tightly coupled loops can also be well suited for double resonance [32], though it can be complicated to get good efficiency on both coils [16]. With either the multiply tuned single loop or the tightly coupled coplanar loops, detailed circuit simulations [8] are generally essential to achieve the desired balance of rf efficiencies at the different frequencies.

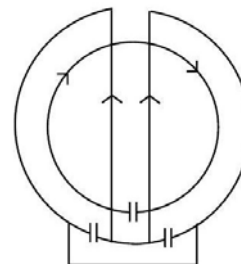


Figure 7. Quadrature surface coil from the combination of a pair of D coils and a loop. The current direction is shown with the arrows.

Catheter coils, intra-cavity coils, and surgically implanted coils, like conventional surface coils, provide greatly enhanced local sensitivity compared to volume coils [21, 32, 33]. They have seen increasing use in human applications, including double-resonance prostate coils [32, 34], and there are indications they may begin to see use in small-animal applications.

**Linear-Polarization Volume Coils.** Solenoids were the mainstay of NMR receiver coils in the early days for a very simple reason – they permit the highest S/N when sample losses are not dominant and  $B_0$  homogeneity is not critical [35]. They also can achieve very high  $B_1$  homogeneity. With the advent of superconducting magnets, saddle coils supplanted solenoids for most NMR spectroscopy for two compelling reasons: they permit much higher spectral resolution, and they are compatible with automatic sample exchange [35, 36]. Perhaps the strongest advantage of the multi-turn saddle coil [37] is that two of them can be oriented orthogonally with excellent performance of each in double-resonance experiments.

As magnets progressed to higher fields, it was seen that the S/N disadvantage of the saddle coil compared to the solenoid was not as great as was originally thought – especially for large, single-tuned,  $^1\text{H}$  applications where sample losses dominated. The Alderman-Grant coil [38], as shown in **Figure 8**, demonstrated that capacitive segmentation was a very effective method of dramatically reducing sample losses because the voltage builds up only over half of the inductance of a similar one-turn saddle coil before it gets reversed by a segmenting capacitor. Also, the quadrupolar symmetry of the conservative  $\mathbf{E}$  field reduces its average value throughout the sample. Numerical optimization by Kost showed that the optimum subtended angle of the window was about  $90^\circ$  for best  $B_1$  homogeneity [39], though it still left much to be desired.

Both multi-turn saddle coils and solenoids continue to be the coil of choice for many applications, especially in NMR spectroscopy [40, 41]. The micro-solenoid, which has only very recently been well understood [8, 40], is usually preferred for sample sizes below 3 mm; and the multi-turn saddle coil is usually the volume coil of choice for  $fd$  in the range of 2-6 MHz-m for double resonance – and sometimes as high as 10 MHz-m. The Alderman-Grant coil has often been used for the 5-15 MHz-m range – usually with a mean subtended angle of  $\sim 120^\circ$  for improved orthogonal flux transparency when an orthogonal coil is needed for double resonance.

The primary limitations of the Alderman-Grant coil are limited  $B_1$  homogeneity and poor transverse flux transparency. These limitations may be solved by using parallel conductors with insulated crossovers in a way that forces a more optimal surface current distribution [42, 43]. At the same time, both  $Q_L$  and  $\eta_F$  may be improved, and the capacitive segmentation may be extended for improved tuning with larger samples at higher frequencies. Coils with parallel conductors with insulated crossovers have been denoted Litz coils.

The primary surface pattern, as shown in **Figure 9** laid out flat, is the basic version of what has been denoted the Center-fed One-turn Litz coil (CF1T) [42, 43, 44]. This is the simplest, significant improvement on the Kost optimization [39] of the slotted resonator [45], or single-turn saddle coil [46], to which its inductance is similar. There are two parallel paths on each side of this coil with an insulated crossover (not fully shown) such that each path, by symmetry, has the same inductance. Hence, each path carries the same current, irrespective of the azimuthal locations, axial locations, or frequency. The azimuthal locations

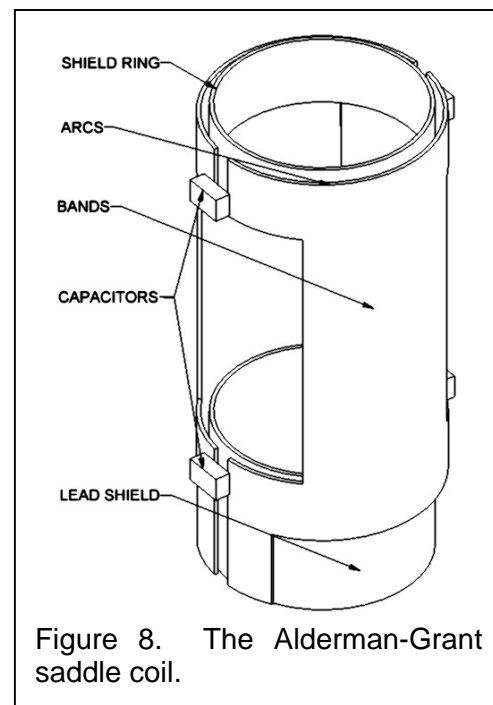


Figure 8. The Alderman-Grant saddle coil.

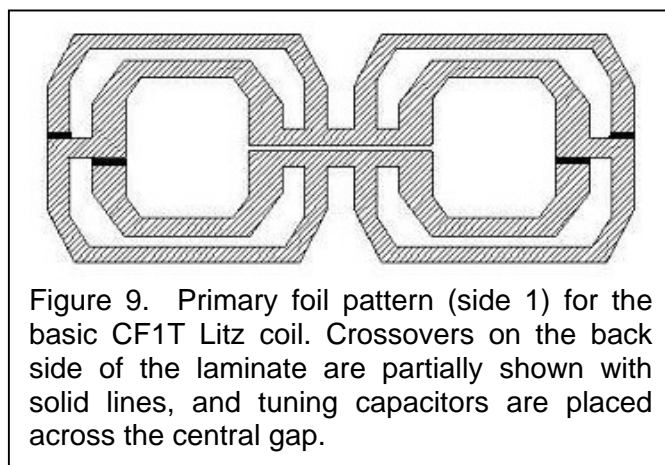


Figure 9. Primary foil pattern (side 1) for the basic CF1T Litz coil. Crossovers on the back side of the laminate are partially shown with solid lines, and tuning capacitors are placed across the central gap.

are chosen for a balanced optimization of  $B_1$  homogeneity,  $\eta_F$ , and  $Q$ . With typical foil widths, the optimum mean azimuthal locations of the inner and outer loops are  $91^\circ$  and  $156^\circ$ . Compared to the Kost coil, the diameter of the homogeneous sample volume (6% rms inhomogeneity) is increased from 65% to 78% of the coil's diameter, the  $Q$  is increased by  $\sim 15\%$ , and the coil has excellent transparency to transverse rf flux. The filling factor is increased by over 40%, primarily because of the large increase in the homogeneous volume. As it is not capacitively segmented, its performance is usually sub-optimal for single-resonance, fixed-frequency applications above  $\sim 5$  MHz-m. However, it is often the best choice for  $fd$  in the range of 3-11 MHz-m when a wide tuning range is desired, such as  $^{31}\text{P}$  to  $^{13}\text{C}$  for mouse and rat applications at 4.7 to 14 T. (Recent simulations of more complex versions of this coil [43], with more parallel paths and more crossovers, show such to offer little advantage.) Of course, there is significant capacitance between the two parallel paths at the crossovers, and this introduces a parasitic high-frequency mode that can be near the  $^1\text{H}$  frequency in double resonance. Also, as the coil has rather low inductance (for example,  $\sim 26$  nH for a short 30 mm coil inside a large shield) lead losses can be fairly substantial if not properly addressed when multi-nuclear tuning is desired. As with the surface coil, detailed rf circuit modeling is useful. A balanced transmission line, such as a twisted pair, from the coil

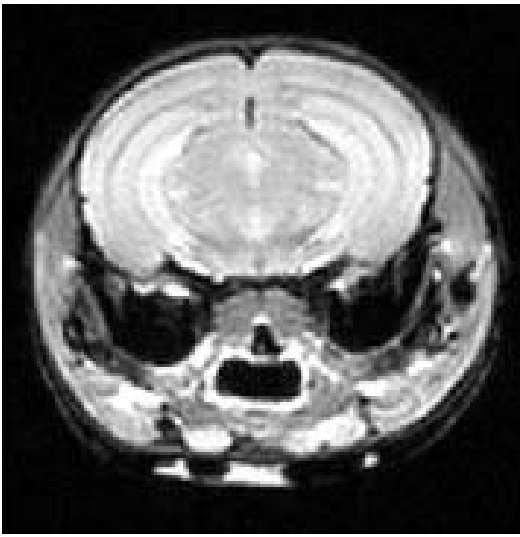


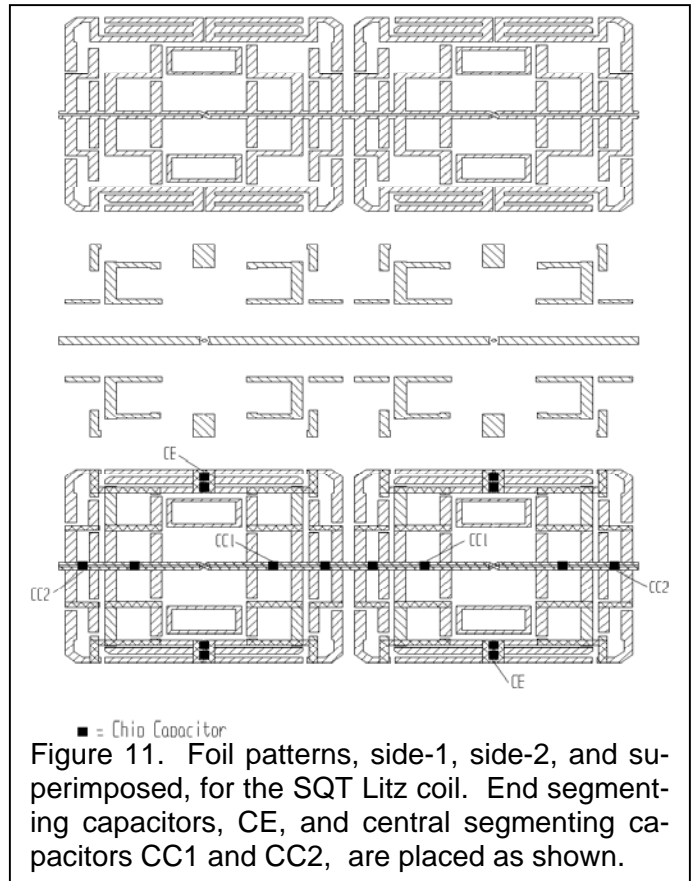
Figure 10. Live mouse brain at 4.7 T, linear litz coil (Biomedical MR Laboratory, Washington University, St. Louis, MO).

to the matching network generally gives better results than other options.

The 24 mm linear coil shown in Figure 9 achieves  $20 \mu\text{s}$   $^1\text{H}$  pw90 for a hard 50 W pulse for mouse

head imaging at 4.7 T – which is better than obtained with birdcages. In-plane resolution, as shown in **Figure 10**, of  $175 \mu\text{m}$  is readily obtained for a T2-weighted, spin-echo, multi-slice experiment, no contrast agent,  $128 \times 128$ , 0.4 mm slice (12 nL voxel),  $T_R = 3$  s,  $T_E = 20$  ms, NEX=1.

It is possible to further improve  $B_1$  homogeneity and extend the useful range by capacitive segmentation and more parallel current paths in which the currents are optimally controlled. **Figure 11** illustrates the foil patterns, laid out flat, for what has been designated the Symmetric Quarter Turn (SQT) (Doty) Litz coil (the current paths execute a quarter turn around the  $B_1$  axis before their inductance is capacitively negated). The homogeneous  $B_1$  region extends radially to 84% of the coil diameter and axially to the inside of the arcs on which the end-segmenting capacitors, CE, are mounted. (Note that the isolated closed loops in the ends of the central flux windows improve  $B_1$  homogeneity by reducing the peak fields otherwise seen in these areas. Otherwise, the coil is quite similar to one previously described in detail [42].) Both  $B_1$  homogeneity and S/N of this linear coil are often better than that of the 16-rung CP birdcage for closely shielded cases with long samples (extending well beyond the coil) with  $fd$  below 20 MHz-m [47]. For example, a 16 cm SQT coil at 3 T proved superior to circular-polarization (CP) birdcages and TEM resonators of similar dimensions [47]. It is instructive to point out that the unloaded to loaded  $Q$  ratio in the CP coils exceeded three, and still the linear coil achieved higher



■ = Chio Capacitor  
Figure 11. Foil patterns, side-1, side-2, and superimposed, for the SQT Litz coil. End segmenting capacitors, CE, and central segmenting capacitors CC1 and CC2, are placed as shown.

S/N. Another useful attribute of this coil is that it may be tuned over a relatively wide range (compared to the birdcage) with little degradation in  $B_1$  homogeneity or S/N, as it does not rely on capacitive phase shifts to achieve the desired current distribution. This coil (or one very similar) has been used in numerous applications from 18 mm at 600 MHz to 160 mm at 125 MHz. In some cases, they have been tunable from  $^{19}\text{F}$  to  $^1\text{H}$ .

The primary disadvantage of the SQT coil is the extra axial space required at the ends (needed to achieve the reduced current concentrations there), as this prevents it from being effective for head coils – whether for mouse or man. Another disadvantage is that the segmenting chip capacitors needed at the center of the coil may lead to shimming artifacts for coils below 20 mm diameter. Yet another drawback is that since much of the surface is covered by the copper foil pattern, it is not as easy to see the sample through the coil – a desirable feature in working with small animals. This is not important in closely shielded rf coil modules, as the shield naturally is opaque, but the more convenient approach for small animals in horizontal-bore magnets is a platform with removable rf shield and full access to the coil and animal. Hence, the birdcage, or a derivative as discussed in the next section, is often selected even where the SQT might provide higher S/N – such as for mouse liver up to 400 MHz and rat liver up to 200 MHz.

The SQT coil has often been used for the  $^1\text{H}$  channel in double-resonance for  $fd$  in the range of 5-20 MHz-m with an orthogonal CF1T Litz coil for the low-frequency channel. Couplings between the orthogonal coils generally limit this approach to 25 MHz-m.

**Circular Polarization (CP) Volume Coils.** The birdcage is arguably the ideal volume coil for generating uniform circular polarization, which generally allows a 40% increase in S/N compared to linear polarization from the same coil, as well as a factor of two reduction in specific absorption rate (**SAR**) [48-51]. Because the birdcage and its common variants (low-pass, balanced low-pass (**BLP**), balanced high pass (**BHP**), high-pass) have been discussed and analyzed in numerous papers over the past two decades [4, 51-55], it will not be reviewed here. Rather, we'll mention only a few points that are particularly interesting to small animal applications and then look a little more closely at a recent variant that is particularly useful for many small-animal applications – the Litzcage<sup>TM</sup>.

Much smaller capacitances are generally needed in birdcages for small animal applications than in common human applications. Consequently, the effects of stray capacitances are often relatively greater in small-animal coils, and the problem is exacerbated by the fact that  $Q_s$  are much higher. Accommodating wide ranges of loads presents challenges for small CP coils at high fields.

Tropp has shown, both theoretically and experimentally [53, 55], that symmetry in the birdcage is *not* critical for the case of the human head at 3T and higher, where the  $fd$  product is 30 MHz-m or greater, as in such cases dielectric resonance effects within the sample have dominant effects on the field profiles. However, this is not the case for most small-animal applications, where  $fd$  is usually less than 20 MHz-m and often as small as 5 MHz-m (mouse at 200 MHz). For such cases, tuning symmetry is quite important.

Even with perfect symmetry, at least 12 rungs are generally required for adequate  $B_1$  homogeneity in a closely shielded small birdcage when a relatively large region of uniformity (**ROI**) is needed. Such coils typically have an easy tuning range of less than 1% with good homogeneity and channel separation, while sample tuning shifts can be as large as 8% for the small, heavily loaded birdcage. However, the 8-section birdcage is about twice as robust (tunable and correctable) as the 12-section birdcage, partly because it is possible to attach two adjustment variables to nodes at  $45^\circ$  with respect to the feed planes, which simplifies the symmetrization problem when tuning to different loads. Corrections in the 12-rung birdcage, on the other hand, tend to mix more with all tune and match adjustments, which complicates the process. While the  $45^\circ$  nodes are available in the 16-section birdcage, it has twice as many distinct capacitors and usually about half the tuning range.

Crozier observed that capacitor losses are usually rather significant in small birdcages, and for this reason the small 8-section coil (at 200-750 MHz) usually has higher  $Q$  and S/N than the 12- or 16-section small coil [56], an observation confirmed by many others [57]. He also showed that a significant increase in the usable  $fd$  limit and  $Q$  of the 8-section high-pass birdcage could be obtained by using two bands in parallel in each section rather than a single wide rung [56]. With a single wide rung, most of the current flows near the edges, so removing the copper from its center has little effect on copper losses, while it reduces electric field couplings to the sample and thus improves the  $Q$ . Still its homogeneity is that of the 8-rung coil, and it is degraded by the fact that the current in a birdcage always crowds to the worst side of the rungs. For

example, when the rotating  $B_1$  is aligned with X, the current crowds to the edges of the rungs closer to the XZ plane. When the phase is aligned with Y, the current crowds to the edges closer to the YZ plane. In an 8-section birdcage, the effect is quite pronounced.

Varian has demonstrated that small birdcages with even more than 16 rungs can be produced by integrating the capacitors into the double-clad low-loss laminate [58]. These Millipede™ coils have demonstrated exceptional  $B_1$  homogeneity in small coils with mineral-oil samples [58]. They have also demonstrated impressive images in a multiple-mouse application with high dosage of contrast agent at 7 T [59], but details of the rf performance of the current products are not readily available. One advantage of this approach is that it reduces the susceptibility artifacts from chip capacitors in very small coils.

Another recent avenue being pursued by Varian is (effectively) ultra-thickening of the conductors in the conventional birdcage by bending and extending the conductor foil edges in the radial direction [57]. They report an 8-rung, 550 MHz, 7 mm example in which the radial thickness of the conductors is 30% of the coil inner radius  $r_1$  and the shield radius  $r_2$  is  $3r_1$ . Here, compared to a reference thin-foil 12-rung case with the same  $r_1$  and  $r_2$ , a 50% improvement in Q with a 20% loss in filling factor (for a constant sample volume) was obtained, giving a 15% gain in S/N, but with a substantial loss in  $B_1$  homogeneity. Similar approaches have been discussed and evaluated by various researchers [43], but usually there is not enough space available between the coil and an outer coil or the shield for such an approach to be practical.

The TEM coil is a favorite by many researchers in high-field human applications [53, 60], and the strip-line variant has been used in some small-animal applications [61]. A recent analysis using multi-conductor transmission line theory achieved remarkable agreement between experiments and theory in predicting unloaded mode frequencies for a number of linearly driven cases, including 7.5 cm at 200 MHz and 13.4 cm at 300 MHz [62]. Apparently, it is quite difficult to achieve satisfactory quadrature operation in such coils for small animal applications with slotted rf shields. This is at least partly because the inhomogeneous modes are closer than in the birdcage and its derivatives [53]. Our experience suggests this difficulty in achieving clean quadrature tuning (at least for  $fd > 12$  MHz-m) also frequently extends to the BLP birdcage, which is topologically similar to the TEM and stripline coils. While additional modes not present in the isolated BHP birdcage also appear when it is coupled and matched, the matching methods presented shortly are more robust and predictable with this topology.

The homogeneity of the Crozier coil may be improved by inserting an insulated crossover at the center of each pair of rungs, as shown in **Figure 12**, in what has been denoted the Litzcage [63, 64]. The central crossover (by symmetry) forces the current to be equal in each of the two parallel paths in that section, which gives a significant improvement in  $B_1$  homogeneity over the alternative 8-section CP coils (either a single wide rung or the Crozier version), in which the current concentrates on the side closer to the rotating  $B_1$  axis. With the crossovers between the parallel paths, the currents are always equally divided between the two parallel paths and  $B_1$  homogeneity is improved for cases well below dielectric resonance conditions – i.e., for  $fd$  less than  $\sim 20$  MHz-m. **Figure 13** compares the calculated  $B_1$  map for the Crozier coil and litzcage for a 25 mm coil at 300 MHz.

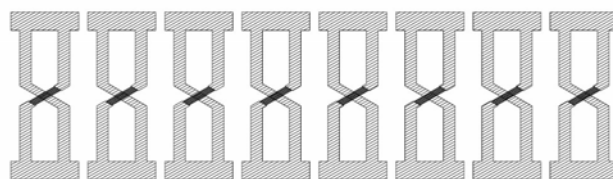


Figure 12. An approximation of one surface of the high-pass Litzcage foil pattern. Insulated crossovers are shown with solid lines.

From an rf circuit perspective, the homogeneous mode is almost indistinguishable from that of Crozier's parallel-rung 8-section birdcage [56], which is of course quite similar to the conventional birdcage.

However, the 30% reduction in stray capacitance in the litzcage (relative to the 8-rung birdcage) allows it to tune ~15% higher. The Litzcage has homogeneity and S/N at least as good as that of the ideal 12-rung birdcage while retaining the tuning ease and robustness of the 8-rung birdcage.

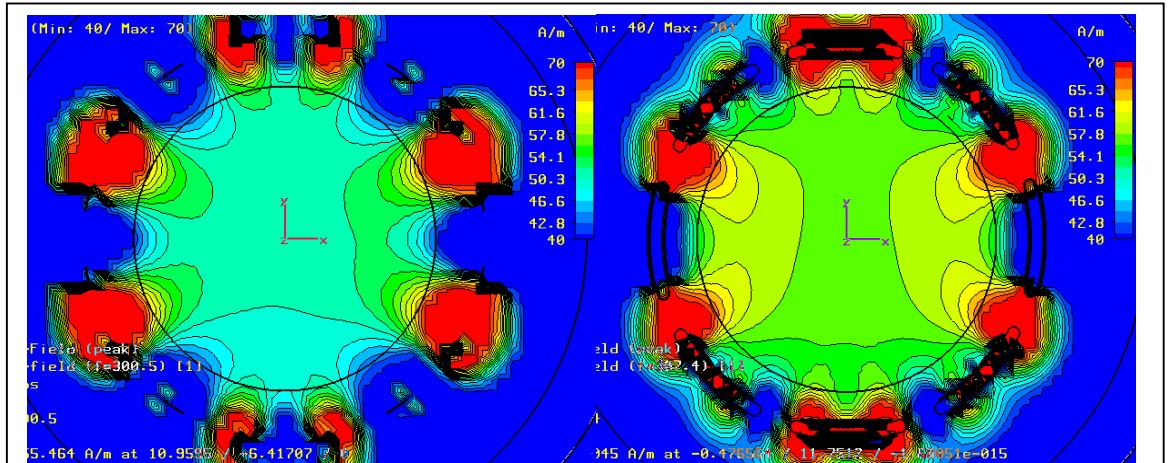


Figure 13.  $B_1$  field in the central xy-plane for the Crozier coil (left) compared to the Litzcage (right) for low  $fd$  ( $f=300$  MHz,  $d=25$ mm). The mean field strength is ~10% higher for the litzcage and inhomogeneities near the rungs are less. Contour increments are approximately 2.5% of the central value.

The 8-section Litzcage has been used at  $fd$  up to 41 MHz-m (20.5 cm, 200 MHz), but the 16-section BHP birdcage is generally a better choice beyond 25 MHz-m, especially in larger coils, where the extra modes caused by the crossovers can get in the way. Also, with the central crossovers, accurate 3D full-wave simulations are much more computationally intensive.

As discussed earlier, S/N is proportional to  $B_1/P_i^{1/2}$  (This also is one of the best methods of evaluating the accuracy of MRI RF coil simulation software.) NMR measurements on a 21 mm diameter, 20 mm length, 750 MHz litzcage yielded a  $90^\circ$  pulse length of 22  $\mu$ s for a square 50 W pulse on a pure water sample in an 18 mm diameter NMR tube with a  $Q_L$  of 100 [65], which was lower than expected for this coil. We suspect higher than expected rf eddy current losses in the external rf shield contributed to the discrepancy. The external, gradient-transparent, rf shielding is seldom recognized as a significant source of signal loss, but in fact that can be the case for small-animal coils with closely spaced external shields. We have found that the

standard method (overlapping slotted shields on double-clad Duroid laminate) can add very high losses under some conditions. Lower shield losses can often be obtained using single-layer gapped foil with discrete chip capacitors across the gaps in the regions where the azimuthal-rf-current densities are high. (For an excellent study on shield slotting requirements, see [66].)

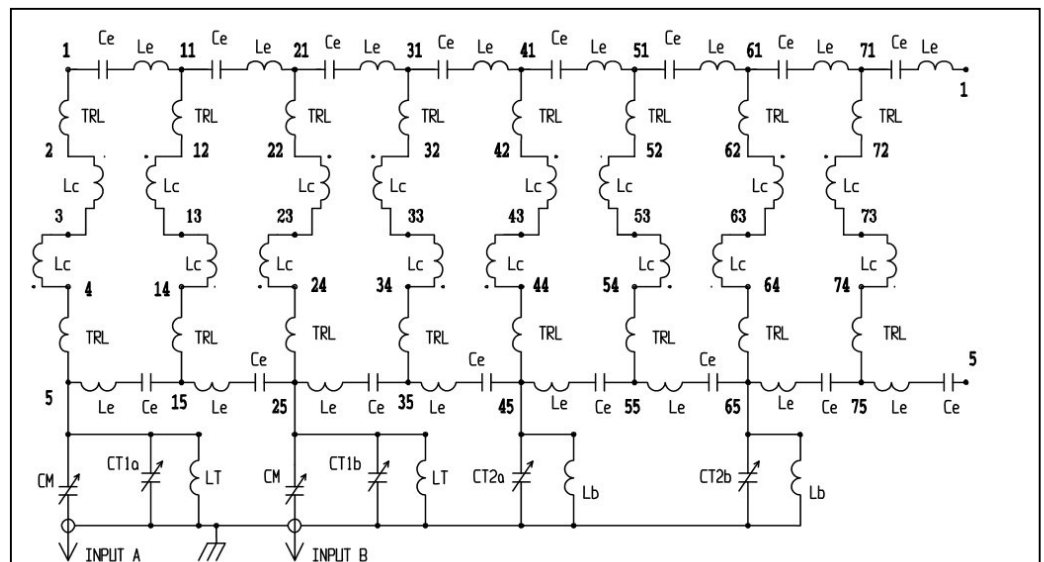
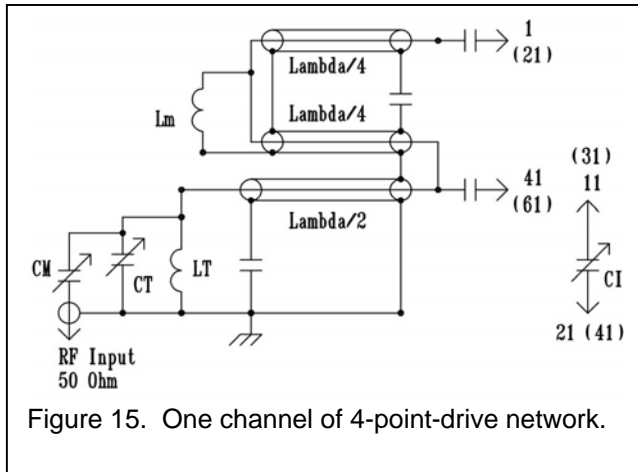


Figure 14. A useful rf circuit model for the 8-section small-animal BHP birdcage. Elements between nodes 1 and 5 correspond to rung 1, between nodes 11 and 15, rung 2, etc. Nodes 1 and 5 on the right are connected to the same on the left.

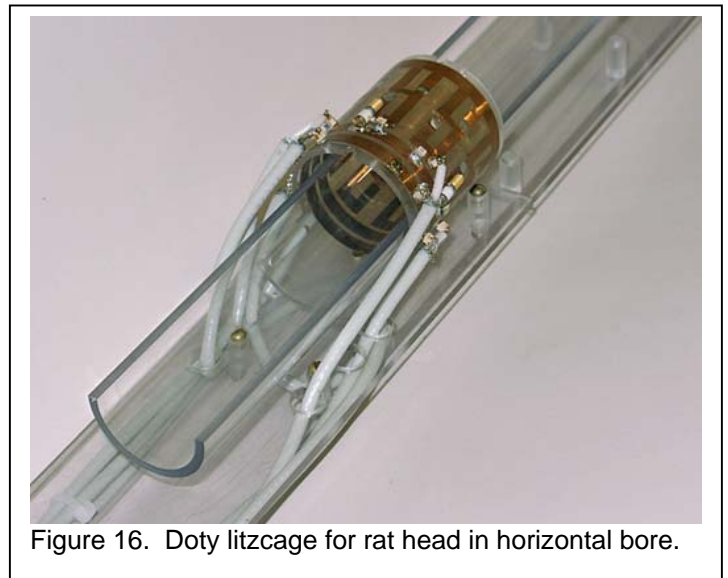
**RF Circuit Models for Small, Tunable, CP Coils.** Several factors conspire to make it difficult to achieve high  $B_1$  homogeneity in small-animal coils. It is sometimes difficult to achieve the necessary precision in the capacitor mounting, or in the uniformity of the shield spacing around the coil. The capacitor accuracy required to place the resonance within the tuning range (the range which keeps the loaded peak-to-peak relative rung current errors below 15%) is very tight for two-point quadrature drive in small, high-frequency birdcages. For an 8-rung BHP birdcage, mean-capacitor-value accuracy must be within 1.5%. A short 18 mm coil of this type (for mouse-brain studies) at 750 MHz requires tuning capacitors of  $\sim 3.9$  pF – including stray, which varies from 0.2-0.5 pF, depending on the sample. Hence, the stray variability exceeds the required tolerance by more than a factor of two, which makes this coil with 2-point-drive problematic. Moreover, the maximum useful tuning range for a small 8-section BHP birdcage with standard 2-point-drive is  $\sim 1.3\%$  - well under typical sample-induced tuning shifts. Four-point-drive networks can achieve up to 5% tuning range with good symmetry and efficiency, but they have more parasitic modes, so it is quite useful to have a good circuit model to be better able to deal with such.



drive is  $\sim 1.3\%$  - well under typical sample-induced tuning shifts. Four-point-drive networks can achieve up to 5% tuning range with good symmetry and efficiency, but they have more parasitic modes, so it is quite useful to have a good circuit model to be better able to deal with such.

**Figure 14** illustrates a simple circuit model that often gives the accuracy needed for the small, 8 rung, BHP birdcage or litzcage. To represent the nearest-rung couplings ( $L_C$ ), each rung includes two ideal transformers, one on either side of the central plane – e.g., rung 2 includes transformers [2,12,3,13] and [13,23,14,24]. A transmission line (TRL) at each end of each rung completes its self-inductance and furnishes most of the stray capacitance per rung (e.g., [11,12] and [14,15] in rung 2). All of the major parasitics are included. Most of the losses appear as corrected attenuation coefficients in the TRLs representing the rungs. Appropriate values for the characteristics of the TRLs and the rung couplings  $L_C$  may be determined adequately by conventional methods.

One-channel of an effective quad-balance network is shown in **Figure 15**. The two series quarter-lambda's force the needed symmetry, greatly improving tuning range with good symmetry and making it easier to achieve adequate channel isolation. The unlabeled capacitors are simply eddy-current-blocking capacitors (rf shorts).  $L_M$  is used to move the common mode well away from the differential mode.  $L_T$  tunes out half of the sum of the tuning variable  $C_T$  and the mean match variable  $C_M$ , thereby doubling the useful tuning range. The half-lambda feed line allows placement of the variable capacitors well away from the coil for maximum openness and access around the coil. With low-loss coaxial lines, the total signal loss added by the balancing network is typically a few percent. An example for the horizontal bore is shown in **Figure 16**. Complex life support and physiological monitoring systems (such as those made by SAll, Stony Brook, <http://www.i4sa.com/index.htm>) may be set up, possibly along with surgical procedures [64], on the live animal. The assembly slides inside an external rf shield.



A 25 mm diameter 300 MHz Litzcage similar to that pictured in Figure 16 permitted 50-micron isotropic resolution (0.125 nL voxel) on four fixed mouse embryos simultaneously, one of which is shown in **Figure 17** [67]. It is important to note that only slightly lower performance would have been achieved with the linear litz coil in this case. The voxel volume reduction of two orders of magnitude compared to Fig. 10 was primarily from (1) the use of a high level of contrast agent, (2) the increased image acquisition time (here, 14.6 hours for the complete 3D data set, rather than a few minutes), (3) the use of a 3D gradient echo sequence, and (4) the higher field.

**Phased Arrays.** In human MRI applications, phased arrays have proven to be extremely advantageous in trading excess S/N for speed and in improving S/N, especially in the periphery [68-70]. Speed-up factors of 2 to 6 are commonly achieved, and higher speed-ups have been achieved. A number of techniques have been developed to take advantage of the improved, localized S/N from an array of surface coils, and perhaps the most successful has been SENSE (SENSitivity Encoding) and related techniques [71]. When sample losses are dominant, the phased array may provide a significant increase in S/N near the surface. Also, the speed up is achieved without severe demands on the gradient hardware (as in EPI). Ideally, the  $S/N^{sen}$  of the SENSE technique relative to the conventional  $S/N^{full}$  using a volume coil is given by

$$S / N^{sen} = \frac{S / N^{full}}{g\sqrt{R}} \quad (8)$$

where  $g$  is a coil geometry factor that is always greater than one and  $R$  is the speed up factor. In general, there will be systematic errors in the coil sensitivity calibration that further degrade S/N, and performance will also be degraded by couplings between the coils. Various methods of both inductive and capacitive decoupling of adjacent coils have been utilized, but the most effective general method is preamplifier decoupling, in which ultra-low-noise preamplifiers with high reflection coefficients and special mismatching networks either detune or severely over-couple the coils [72].

Speed up has been demonstrated in rat brain imaging at 11.7 T using a 4-channel rat head array [73] with a novel approach to adjacent coil decoupling. There have also been other demonstrations of phased arrays in MR microscopy [74] and small-animal imaging [75], and the major vendors have been supplying 4-channel and 8-channel high-field scanners for small-animal applications for several years. SENSE and Generalize Auto-calibrating Partially Parallel Acquisitions (GRAPPA) both offer clear advantages compared to EPI at very high fields. Still, the general applicability of phased arrays in small-animal applications seems somewhat limited, as resolution is usually paramount and is often limited by S/N. This is particularly true in MR spectroscopy [76, 77].

When two coils tuned to the same frequency are coupled, the mutual inductance causes the resonance to split into two modes on either side of the original frequency, and sensitivity at the original frequency is quite low. Roemer showed that preamps with low input impedance may be used to reduce the resonant current and coupling in surface coils for a particular type of matching network (similar to that shown for passive detuning in Figure 3) in which a low preamp impedance is transformed to a high impedance in series with the actual surface coil [69]. The effect is essentially equivalent to placing a preamp of low input impedance between nodes [2, 3] in Figure 3, or a preamp of high input impedance between nodes [12,13]. They note that when a half-lambda line, practical transformation methods, and standard tuned MOSFET (Metal-Oxide-Semiconductor Field-Effect Transistor) preamps are used, the effect on efficiency at 64 MHz is to insert about  $5 \Omega$  in series with the surface coil. The majority of the resistance comes from the circuit elements other than the FET and has thus the same effect on S/N as putting a real  $5 \Omega$  resistor in series with

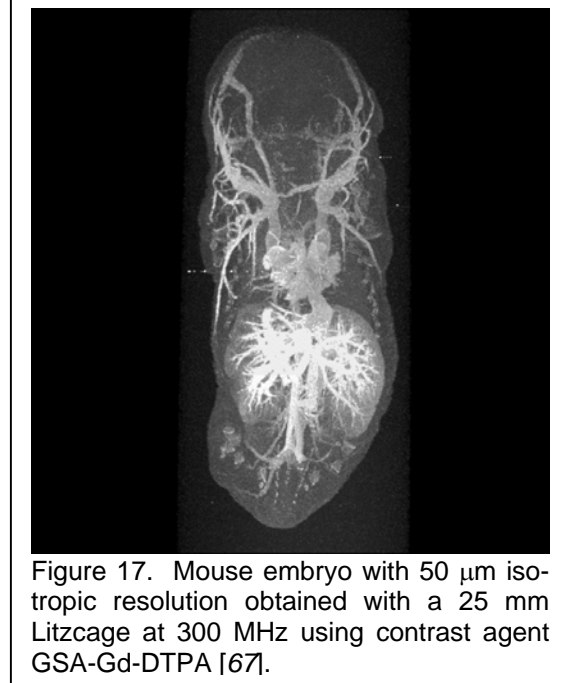


Figure 17. Mouse embryo with 50  $\mu\text{m}$  isotropic resolution obtained with a 25 mm Litzcage at 300 MHz using contrast agent GSA-Gd-DTPA [67].

the coil. This may be acceptable on a large coil, but it can be devastating in a small coil where the series resistance is initially  $\sim 0.5 \Omega$ . Simulations indicate that the loss in a  $\lambda/4$  cable (type 1855) between a maximally decoupled small surface coil at 200-300 MHz (26 nH in series with 10 pF tuning, no matching) and a typical “zero-impedance” ( $\sim 2 \Omega$  input impedance) preamp results in  $\sim 2.5$  dB loss in S/N in just the cable for light-load applications. The impedance transformations and NF (Noise Figure) in commercially available preamps can lose another 2 dB.

Others have noted the limitations of Roemer’s initial approach to preamp decoupling for small coils and have shown that there are better and more flexible schemes that simultaneously achieve low resonant currents in the surface coils and improved noise match [72], but the analytical approaches still often include significant assumptions – lossless matching components and infinitesimal transmission line lengths. With small coils at high fields it is important to fully include all losses in the various transformations (at the coil, at the preamp input, and there between) in detailed numerical circuit simulations.

It is possible that some published performance gains with phased arrays of small coils have been based on comparisons to sub-optimal conventional coils. Clearly, there are many ways to inadvertently get performance from a small reference surface coil or volume coil that is below optimum; and having a small coil sample-noise dominated may be a sign of excessive conservative-E-field losses [8], as was seen earlier in Table 1.

There is a need for improved methods of assessing the performance of phased arrays, as g-factors and noise correlations tell one only how quickly the coil degrades with increasing speed-up factors. The g-factor gives no insight as to how the starting point performance ( $R=1$ ) compares to a well optimized homogeneous coil. Moreover, since it is usually impractical to operate a phased array in transmit mode, phased arrays have seldom been evaluated from the perspective of reciprocity. The importance of being more quantitative about S/N performance of phased arrays has recently stimulated several groups to develop improved methods of calculating ultimate attainable S/N for large MR phased arrays [78, 79, 80], where losses in the coils, capacitors, transformation networks, and preamps are all more easily made negligible.

The common-mode or “cable” problems, briefly discussed earlier under surface coils, become more challenging with phased arrays, but more effective solutions are beginning to appear. Local high-gain preamps with optical links are being investigated [81]. It currently appears that the NF of a direct modulation optical link is likely to be  $\sim 29$  dB, so a local coil preamp with  $\sim 40$  dB of gain is needed to prevent significant degradation in NF [81]. Achieving the needed dynamic range in the high gain, low noise preamp is a major challenge. Local coil preamps with all the control, power, and signal on a single coax cable are currently more practical and promise a substantial benefit by allowing more flexibility in dealing with cable modes without these measures degrading S/N [82].

The need for special preamps integrated into the array coil package near the animal adds a substantial amount to its cost. While this cost is clearly justified in many human imaging applications, other options may often be superior to phased arrays in small animal coils. These options include conventional CP volume coils with improved optimization for the ROI, more fully optimized surface coils, and cryogenic coils. But having said this, there are nonetheless many places where phased arrays provide substantial advantages in small-animal studies, and it is important to appreciate their requirements.

**Ultra-low-noise Mismatched Preamps.** To achieve significant S/N gains for many interesting cases – for preamp-isolated phased arrays, or for cryogenically cooled coils – ultra-low-noise preamps are needed, and perhaps at unusual input impedance. The tuned preamps normally used in  $^1\text{H}$  MRI typically achieve NF of about 0.4 dB (not including input line losses) when noise matched, though long rf lines can easily add 1 dB to the NF even when VSWR is low. The cable losses are greater with phased arrays when the reflection coefficients at both ends of the line are high. Some appreciation for the real effects of mismatching and “lossless” transformations may be gained from a reported case at 0.5 T (21 MHz). Here, the effect of a typical “lossless”  $90^\circ$  hybrid and minimal  $n\lambda/2$  cable lengths (probably  $\sim 5$  m) was to reduce S/N by 3.3 dB for a factor-of-4 impedance mismatch to a preamp with 0.5 dB NF (when optimally noise matched) [83]. In this particular case, the mismatch was not deliberate for coil decoupling but rather was a result of an absence of suitable coil matching circuitry.

For the case of coil decoupling, much greater mismatching is required. For coil coupling coefficients of 0.01 (a typical value for adjacent coils without extremely careful inductive or capacitive decoupling) with individual loaded  $Q_L$  of 50, a *minimum* of a factor-of-10 over-coupling would be needed for low noise

correlation between the coupled coils. Extreme over-coupling places severe requirements on the preamp's NF, whether the coil is matched by parallel or series or mixed elements [84].

The lowest NF is currently obtained with Enhancement mode Pseudomorphic High Electron Mobility Transistors (E-PHEMT) – a fairly recent GaAs (Gallium Arsenide) device. The ATF-58143 has NF<sub>min</sub> below 0.13 dB (at 25°C, zero magnetic field) at frequencies below 500 MHz when matched at the optimum (frequency dependent) input reflection coefficient [85]. It also has very low intermodulation distortion and saturated output power of 12 dBm. Accurate simulations of complex circuits containing active devices are readily carried out with standard circuit software if their S-parameters and noise parameters are known at the frequencies of interest. The pulse-protected simplified preamp circuit shown in **Figure 18** can achieve NF under 0.3 dB with over 20 dB gain at 300 MHz when noise matched for line impedances of 25-100 Ω, but stabilization is more complicated than suggested by this simplified schematic.

Equation (4) is still valid for the unmatched or detuned coil as long as all the losses between the preamp and the coil are included in the coil circuit simulation and the preamp noise temperature is small compared to the dominant coil noise temperature. The coil/preamp system optimization may be addressed by picking a convenient point in the transmission line between the coil and preamp for splitting the coil circuit problem from the preamp problem. Simulating the coil circuit (including transmission lines, matching, etc.) from that point to the coil allows one to determine the coil circuit impedance at that point in the line and all losses between there and the coil for the mismatched condition. (A complication in circuit simulation of phased array coils is determining the circuit component losses accurately for the severely mismatched case, as the power actually absorbed at the excitation port in the simulation will be a very small fraction of the incident power and it will be strongly influenced by component losses.) That impedance can then be used as the input port impedance in the preamp simulation, from which its NF may be accurately determined for that source impedance. **Figure 19** shows the NF and gain of the preamp of Figure 18 as a function of input resistance as calculated by the GENESYS “core” linear circuit simulator for the case when the preamp input matching is optimized for minimum NF with a 20 Ω source. Input absolute S<sub>11</sub> (reflection coefficient) at optimum noise match at 300 MHz is ~0.3 and input impedance is 18 Ω at 28°.

The S/N loss in the preamp-decoupled coil is the sum of the losses (in dB) in the coil mismatching circuit (with transmission lines) and the NF of the mismatched preamp. With proper optimization, this sum may be below 1.5 dB even at high fields with adequate coil decoupling; but with insuf-

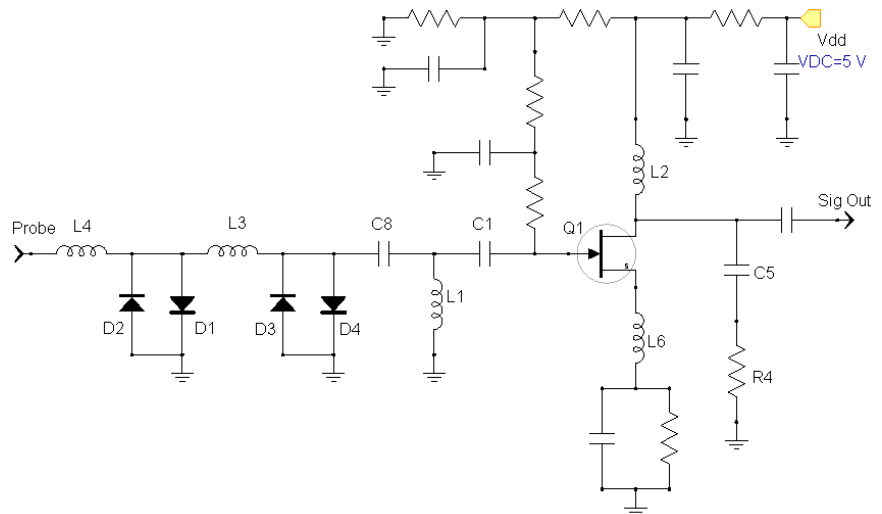


Figure 18. A ATF-58143 E-PHEMT 300 MHz pulse-protected preamp can achieve total NF under 0.3 dB (excluding input cable losses). The source inductor L6 (4 nH) and the output RC network improve stability. Two sets of crossed diodes with inductors L3 (13 nH) and L4 (25 nH) may be needed for adequate input pulse protection. Noise matching is largely determined by C8 (2.2 pF) and L1 (65 nH).

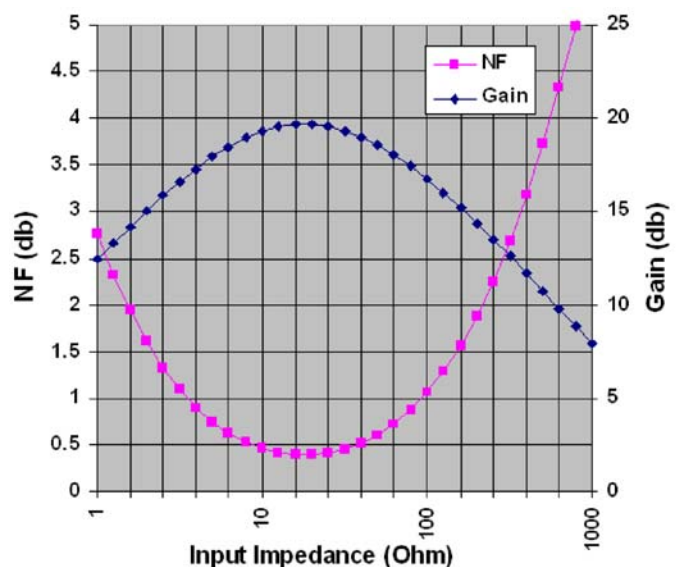


Figure 19. NF and gain of the 300 MHz E-PHEMT preamp of Figure 18 as a function of source resistance when optimized for 20 Ω.

ficient attention to the circuit details, it can easily exceed 6 dB for small coils. Because of their higher  $Q_s$ , the demands in the impedance transformation network can be an order of magnitude more stringent for small coils than for large coils.

The effective, over-coupled  $Q$  may be seen by combining (connecting) the two separate simulations and applying a small “tickler” signal (via a large resistor or a small mutual coupling) to the sample coil. For adequate decoupling, the coil/preamp circuit usually needs to show an effective  $Q$  at the output of the preamp (the  $S_{21}$  response, where  $S_{21}$  is the forward transmission coefficient) below 5 – possibly below 2, depending on coil coupling coefficients. (Note that the standard “impedance matched” condition will often show an effective  $Q$  of nearly twice the coil's  $Q_L$  because of the high reflection coefficient of low noise preamps.)

There are a number of ways to over-couple the coil, but some are better than others [72, 84]. For a small series-matched 300 MHz light-load 16 mm surface coil (with  $Q_L$  of 60), a factor-of-20 over-coupling (i.e., coil transformed to  $2.5 \Omega$  resistive at the preamp input port) gave an effective  $Q_L$  of 8 at the output of a  $50 \Omega$  preamp (similar to that of Figure 18) with an NF of 2.8 dB at  $2.5 \Omega$ . With a half-lambda low-loss cable (type 1855, 0.41 m) between the surface coil and the preamp, the losses in the cable are  $\sim 1$  dB. However, when the same coil is parallel-matched to  $120 \Omega$  resistive, a similar effective  $Q_L$  is achieved with the  $20 \Omega$  preamp of Figure 18. In this case, the preamp NF (at  $125 \Omega$ ) is  $\sim 1.25$  dB and cable losses are only 0.15 dB. One can also use a series-parallel-match, similar to that shown in Figure 3, with impedance  $50 \Omega$  at  $85^\circ$  phase angle, to get similar effective  $Q_L$ , but both cable losses and NF are significantly increased compared to the parallel-matched (high-resistance) case of a preamp of moderately low impedance. Using  $\lambda/8$  rather than  $\lambda/2$  cables for the above, with proper adjustments in the tuning, reduces cable losses by about a factor of 3. However, the NF of GaAs FET and PHEMT preamps increases when placed in fields above  $\sim 7$  T, so it may be preferable to use a full  $\lambda$  cable length so the preamp can be positioned in a region of lower field.

Note that the simple alternative of reducing the effective  $Q_L$  of the surface coil by an order of magnitude by inserting a suitable resistor in series with it would reduce the S/N by  $\sim 10$  dB, and applying Roemer's original  $(2n-1)\lambda/4$  approach with a preamp of very low input impedance to small surface coils could result in a 6 dB (or more) loss in S/N, even though tuned preamps of  $2 \Omega$  input impedance are now commercially available with fairly low NF for frequencies up to 300 MHz [86]. Clearly, it is essential to carry out detailed circuit simulations of the coil/cable/matching/preamp system for small phased arrays.

**Cryogenically Cooled RF Coils.** Bruker and Varian have been producing Cryoprobes for high-resolution NMR on liquid samples of 3 to 5 mm diameter for more than six years, and their factor-of-four gain in S/N is revolutionizing the field of NMR [87]. Recently, similar, linear-polarization, 5 mm micro-imaging cryoprobes for use in vertical-bore 400 MHz magnets have been introduced, and S/N gains up to a factor of four are seen with small, low-loss samples. Bruker has also very recently announced preliminary results from a cryogenic rf platform for *in vivo* mouse brain in horizontal-bore magnets that uses a cryogenically cooled High Temperature Superconductor (HTS) surface coil [88]. They reported a factor of 2.4 gain in S/N compared to a 20 mm quadrature room-temperature surface coil at 9.4 T with active detuning. Other approaches for the use of HTS coils in MR microscopy have also been explored [9, 89-91].

As noted earlier, the noise voltage is proportional to the square root of the product of the resistance and temperature. Reducing the temperature of a copper coil and its rf shield from 300 K to 50 K reduces its rf resistance by typically a factor of four, but the  $Q_s$  of the capacitors may not improve much. Hence, when sample losses are small, the total  $Q$  may improve by about a factor of 3. However, the noise temperature of the coil and capacitor losses is also reduced by a factor of six, so the total noise voltage from the coil, capacitors, and shield may be reduced by more than a factor of 4. To take full advantage of the reduced noise temperature of the coil and capacitors, the preamp (with its input transmission line) must have a noise temperature that is much less than 50 K (0.7 dB). Cooling the preamp to reduce its NF below 0.2 dB is generally justified; but it is just as important to position it very close to the coil, as 1 m of low-loss cable at 300 MHz adds a comparable amount to the effective NF [7].

Both experiments and simulations show that sample losses are nearly comparable to coil and capacitor losses for the case of rat head  $^1\text{H}$  imaging at 400 MHz with a short, 38 mm litzcage or Crozier birdcage, so cryogenic cooling of the coil should increase its S/N by 40%. For mouse brain at 300 MHz, sample losses in a small birdcage may be only 10% of coil and capacitor losses, so a factor of three gain in S/N may be possible. Sample losses increase somewhat more rapidly than quadratically with frequency, so for  $^{13}\text{C}$  MR on rat brains at 9.4 T, there appears to be the potential for a factor of 4 increase in S/N. Relative coil and capacitor

losses in small double-resonance CP coils are typically 2 to 3 times those in single-resonance coils. Hence, there is even more potential for gain in S/N on  $^{13}\text{C}$  in double-resonance  $^1\text{H}/^{13}\text{C}$  applications using cryogenically cooled coils. Undoubtedly, technical progress can be expected in this area in the future.

## Conclusion

The technological advances in mid-range MR RF coils of the past two decades have helped fuel the rapid growth in the field of pre-clinical or small-animal MRI. In this regime, all the sources of loss (coil, capacitor, sample, shield, and transmission lines) are important. All such losses may be accurately captured in some modern full-wave 3D EM software, and these tools permit improved coil optimizations. Standard linear circuit simulators, such as SPICE and GENESYS, have been shown to be useful in optimization of complex coil tuning and matching circuits. Such simulators are also useful for optimal mismatching of ultra-low-noise preamps based on the E-PHEMT, as needed for coil decoupling in phased arrays.

Many coil applications that were considered quite challenging just a few years ago are now considered routine, but the relentless quest for increased speed and S/N continues to bring new challenges and new opportunities. Both full-wave field simulations and linear-circuit simulations are likely to play an increasingly important role in future advances in MR rf coil technology – especially in phased arrays and in cryogenically cooled rf coils, both of which currently seem to hold more promise than advances in magnet technology. While there appears to be limited potential for technological advances in room-temperature mid-range surface and volume coils, there is considerable potential for trading S/N for speed using phased arrays, especially with larger samples. Finally, cryogenically cooled rf coils have revolutionized the field of NMR spectroscopy of liquid samples over the past five years, and they have been shown to offer considerable opportunity for future gains in S/N in  $^1\text{H}$  MRI in small-animal brain studies and in low-gamma applications on larger regions.

Acknowledgements: This work partially supported by NIH R44 EB000445-03 and by Doty Scientific, Inc.

## References

1. Abragam A. *Principles of Nuclear Magnetism*. International Series of Monographs on Physics 32. Oxford Univ. Press: London, 1961.
2. Doty FD. Probe Design and Construction. *The Encycl. of NMR* Vol. 6. Wiley. 1996; 3753-3762.
3. Hoult DI and Richards RE. The Signal-to-Noise Ratio of the NMR Experiment. *J. Magn. Reson.* 1976; **24**: 71-85
4. Doty FD, Entzminger G, Hauck C, and Staab JP. Practical Aspects of Birdcage Coils. *J. Magn. Reson.* 1999; **138**: 144-154.
5. Hoult DI. Sensitivity of the NMR Experiment. *The Encycl. of NMR* Vol. 7, Wiley. 1996; 4256-4266.
6. Tropp JS. Radiation damping and reciprocity in Magnetic Resonance Reception. Presented at *12th ISMRM. Poster 1646. Kyoto.* 2004.
7. Doty FD and Shevgoor S. Beating Reciprocity S/N Expectations in Triple-resonance Narrow-bore MAS by Cryogenic Cooling of Critical Circuit Components in the OptiMAS™ Probe. Poster presented at *Rocky Mountain Conference. Denver.* 2005. [http://www.dotynmr.com/PDF/OptiMAS\\_ENC05.pdf](http://www.dotynmr.com/PDF/OptiMAS_ENC05.pdf) .
8. Doty FD, Kulkarni J, Turner C, Entzminger G, Bielecki A. Using a cross-coil to reduce RF heating by an order of magnitude in triple-resonance multinuclear MAS at high fields. *J. Magn. Reson.* 2006; **182**: 239-253.
9. Brey WW, Edison AS, Nast RE, Rocca JR, Saha S, Withers RS. Design construction and validation of a 1-mm triple-resonance high-temperature-superconducting probe for NMR. *J. Magn. Reson.* 2006; **179**: 290-293.  
[http://www.bme.ufl.edu/documents/edison\\_research\\_article2\\_research.pdf](http://www.bme.ufl.edu/documents/edison_research_article2_research.pdf) .
10. Weiland T. Time Domain Electromagnetic Field Computation with Finite Difference Methods. *Intern. J. of Numerical Modeling.* 1996; **9**: 295-319. Also see: [www.cst.de](http://www.cst.de)
11. Ackerman JJH. Surface (Local) Coils as NMR Receivers. *Concepts in Magn. Reson.* 1990; **2**: 23-42.

12. Hyde J. Surface and Other Local Coils for In Vivo Studies. *The Encycl. Of NMR* Vol. 7, Wiley. 1996; 4656-64.
13. Haase A, Odoj F, Von Kienlin M, Warnking J, Fidler F, Weisser A, Nittka M, Rommel E, Lanz T, Kalusche B, Griswold M. NMR probeheads for in vivo applications. *Concepts Magn. Reson.* 2000; **12**: 361-388.
14. Ackerman JJH, Grove TH, Wong GC, Gadian DG, and Radda GK. Mapping of metabolites in whole animals by  $^{31}\text{P}$  NMR using surface coils. *Nature.* 1980; **283**: 167-170.
15. Edelstein WA, Hardy CJ, and Mueller OM. Electronic Decoupling of Surface-Coil Receivers for NMR Imaging and Spectroscopy. *JMR.* 1986; **67**: 156-161.
16. Mispelter J, Tiffon B, Quiniou E, and Lhoste JM. Optimization of  $^{13}\text{C}$ - $^1\text{H}$  Double Coplanar Surface-Coil Design for the WALTZ-16 Decoupling Sequence. *J. Magn. Reson.*, 1989; **82**: 622-8.
17. Fitzsimmons JR, Brooker HR, and Beck B. A Comparison of Double-Tuned Surface Coils. *Magn. Reson. in Med.* 1989; **10**: 302-309.
18. Peterson DM, Beck BL, Duensing GR, Fitzsimmons JR. Common Mode Signal Rejection Methods for MRI: Reduction of Cable Shield Currents for High Static Magnetic Field Systems. *Concepts in Magn. Reson.* 2003; **Part B, 19B(1)**: 1-8.
19. Misic GJ, Hurst GC, Holland GN, Patrick JL, Orlando PT. Surface Coil System for Magnetic Resonance Imaging. 324/318. *U.S. Pat. 4,920,318, 1990.*
20. Hyde J, Rilling RJ, and Jesmanowicz J. Passive Decoupling of Surface Coils by Pole Insertion. *J. Magn. Reson.* 1990; **89**: 485-95.
21. Zhou X, Maronpot RR, Cofer GP, Hedlund LW, and Johnson GA. Studies on Bromobenzene-Induced Hepatotoxicity Using in Vivo MR Microscopy with Surgically Implanted RF Coils. *Magn. Reson. In Med.* 1994; **31**: 619-27.
22. Suits BH, Garroway AN, and Miller JB. Surface and Gradiometer Coils near a Conducting Body: The Lift-off Effect. *J. Magn. Reson.* 1998; **135**, 373-379.
23. Chen C.-N. and Hoult D. I. Chapters 4 and 5. In *Biomedical Magnetic Resonance Technology*. Adam Hilgar: NY, 1989.
24. deGraaf RA. Chapter 8. *In Vivo NMR Spectroscopy: Principles and Techniques*. Wiley, 1999.
25. Mispelter J. *NMR Probeheads for Biophysical And Biomedical Experiments: Theoretical Principles And Practical Guidelines*. Imperial College Press, 2006.
26. Seeber DA, Jevtic J, Menon A. Floating shield current suppression trap. *Concepts in Magn. Reson.* 2004; **Part B, 21B(1)**: 26-31.
27. Matson GB, Vermathen P and Hill TC. A practical double-tuned  $^1\text{H}/^{31}\text{P}$  quadrature birdcage headcoil optimized for  $^{31}\text{P}$  operation. *MRM.* 1999; **42**: 173-182.
28. Seeber DA. Tuning system for floating radio frequency trap. *U.S. Pat. 6,664,465, 2003.*
29. Wong WH, Leung J, Funk A, Mehr K. Coils for high frequency MRI. *U.S. Pat. 6,980,000, 2005.*
30. Eydelman G, Damadian RV, Giambalvo AJ. MRI Antenna. *U.S. Pat. 6,847,210, 2005.*
31. Mehdizadeh M, Molyneaux DA and Holland GN. Quadrature Surface Coils for Magnetic Resonance Imaging. *U.S. Pat. 4,918,388, 1990.*
32. Karpodinis KG, Carvajal L, Chen AP, Jimenez B, Bruce N, Tropp J, Kurhanewicz J, Vigneron DB. 3T Prostate Coils for  $^1\text{H}$  and  $^{31}\text{P}$  MR Spectroscopic Imaging. Presented at *14<sup>th</sup> ISMRM. Poster 2593. Seattle. 2006.*
33. Farrar CT, Wedeen VJ, and Ackerman JL. Cylindrical Meanderline RF Coil for Intravascular MRI of Atherosclerotic Plaque. *MRM.* 2005; **53**: 226-230.
34. Tropp J, Calderon P, Carvajal L, Karpodinis K, Chen A, Vigneron D, Hurd R, Ardenkjaer-Larsen J-H. An endorectal dual frequency  $^{13}\text{C}$ - $^1\text{H}$  receive only probe for operation at 3.0 tesla. Presented at *14<sup>th</sup> ISMRM. Poster 2594. Seattle. 2006.*
35. Hoult DI. The NMR Receiver: A Description and Analysis of Design. *Progress in NMR Spectrosc.* 1978; **12**: 41-77.
36. Ginsberg DM and Melchner MJ. Optimum Geometry of Saddle Shaped Coils for Generating a Uniform Magnetic Field. *Rev. Sci. Instrum.* 1970; **41**: 122-3.
37. Zens AP. NMR Probe Coil System. *U.S. Pat. 4,398,149, 1983.*
38. Alderman DW and Grant DM. An Efficient Decoupler Coil Design which Reduces Heating in Conductive Samples in Superconducting Spectrometers. *J. Magn. Reson.* 1979; **36**: 447-51.

39. Kost GJ, Anderson SE, Matson GB, and Conboy CB. A Cylindrical-Window NMR Probe with Extended Tuning Range for Studies of the Developing Heart. *J. Magn. Reson.* 1989; **82**: 238-52.
40. Li Y, Webb AG, Saha S, Brey WW, Zachariah C, Edison AS. Comparison of the performance of round and rectangular wire in small solenoids for high-field NMR. *Magn Reson. in Chem.* 2006; **44**: 255-262. [http://www.bme.ufl.edu/documents/edison\\_research\\_article1\\_research.pdf](http://www.bme.ufl.edu/documents/edison_research_article1_research.pdf)
41. Fuks LF, Huang FSC, Carter CM, Edelstein WA, and Roemer PB. Susceptibility, Lineshape, and Shimming in High-Resolution. *J. Magn. Reson.* 1992; **100**: 229-242.
42. Doty FD, Entzminger Jr G, and Hauck CD. Error-Tolerant RF Litz Coils for NMR/ MRI. *J. Magn. Reson.* 1999; **140**: 17-31.
43. Doty FD. Low Inductance Transverse Litz Foil Coils. *U.S. Pat. 6,060,882, 2000.*
44. Doty FD and Entzminger Jr G. Center-fed Paralleled Saddle Coils for Multinuclear Double-Resonance NMR or MRI. *U.S. Pat. 6,175,237, 2001.*
45. Schneider HJ and Dullenkopf P. Slotted tube resonator: A new NMR probe head at high observing frequencies. *Rev. Sci. Instrum.* 1977; **48**: 68-73.
46. Doty FD. Parallel Single Turn Resonator for NMR. *U.S. Pat 4,641,098, 1987.*
47. Doty FD, Bass W, Yang Q, Entzminger G, Wang JH, Doty GN, Holte LL, and Smith MB. The SQT2 Litz Coil - An Exceptionally Robust Knee Coil for 3T. Presented at *10th ISMRM. Honolulu.* 2002. [http://www.dotynmr.com/PDF/KNE\\_SML.pdf](http://www.dotynmr.com/PDF/KNE_SML.pdf)
48. Hayes CE, Edelstein WA, Schenck JF, Mueller OM, and Eash M. An Efficient Highly Homogeneous Radiofrequency Coil for Whole-Body NMR Imaging at 1.5 T. *J. Magn. Reson.* 1985; **63**: 622-8.
49. Edelstein W. RF Systems and Coils for MRI & MRS. *The Encycl. of NMR Vol. 6*, Wiley. 1996; 3950-54.
50. Hayes CE. Birdcage and Other High Homogeneity RF Coils for Whole Body Magnetic Resonance. *The Encycl. of NMR Vol. 2*, Wiley. 1996; 968-974.
51. Tropp J. The Theory of the Bird-Cage Resonator. *J. Magn. Reson.* 1989; **82**: 51-62.
52. Tropp J. Mutual Inductance in the BirdCage Resonator. *JMR.* 1997; **126**: 9-17.
53. Tropp J. Dissipation, Resistance, and Rational Impedance Matching for TEM and Birdcage Resonators. *Concepts in Magn. Reson.* 2002; **15(2)**: 177-188.
54. Leifer MC. Resonant Modes of the Birdcage Coil. *J. Magn. Reson.* 1997; **124**: 51-60.
55. Tropp J. Image brightening in samples of high dielectric constant. *J. Magn. Reson.* 2004; **167**: 12-24.
56. Crozier S, Luescher K, Forbes LK, and Doddrell DM. Optimized Small-Bore, High-Pass Resonator Designs. *J. Magn. Reson. Ser. B.* 1995; **109**: 1-11. Crozier S and Doddrell DM. RF Resonator for NMR. *U. S. Patent # 5,642,048, 1997.*
57. deSwiet T, Wong WH, Romo M, Finnigan J, Burns S. NMR Resonators Optimized for high Q factor. *U.S. Pat. 6,667,674, 2003.*
58. Wong WH, Sukumar S. *Millipede* Imaging Coil Design for High Field Micro Imaging Applications. Presented at *8th ISMRM. Poster 1399. Denver.* 2000.
59. Dazai J, Bock NA, Nieman BJ, Davidson LM, Henkelman RM, and Chen XJ. Multiple Mouse Biological Loading and Monitoring System for MRI. *Magn. Reson. in Med.* 2004; **52**: 709-715.
60. Collins CM, Liu W, Wang J, Gruetter R, Vaughan JT, Ugurbil K and Smith MB. Temperature and SAR Calculations for a Human Head Within Volume and Surface Coils at 64 and 300 MHz. *J. Magn. Reson. Imaging.* 2004; **19**: 650-656.
61. Bogdanov G, Kueppers G, King JA, Ferris CF. Actively tuned dual RF resonator system for functional MRI of small animals. Presented at *9th ISMRM. Poster 1093. Glasgow.* 2001.
62. Bogdanov G and Ludwig R. Coupled Microstrip Line Transverse Electromagnetic Resonator Model for High-Field Magnetic Resonance Imaging. *Magn. Reson. in Med.* 2002; **47**: 579-503.
63. Doty FD, Entzminger G, Rafique Z, Holte L, Welsh T. The Litzcage – a High-field Circular-polarization RF Coil with Improved Tunability, B<sub>1</sub> Homogeneity, and S/N. Poster presented at the *ENC. Asilomar.* 2002. [http://www.dotynmr.com/PDF/RFLC\\_.pdf](http://www.dotynmr.com/PDF/RFLC_.pdf)
64. Doty FD, Laws N, Holte L, Staab JP, Zempel J, and Garbow JR. The 4-point-drive Litzcage - An Semi-open MRI RF CP Coil with a Wide Tuning Range. Poster presented at *11th ISMRM. Toronto.* 2003.
65. Doty FD, Entzminger G, Staab JP, Gravel JD, and Plant HD. Optimization of Homogeneity and S/N in a 750 MHz CP Micro-Imaging Coil. Poster presented at the *44th ENC. Savannah.* April 2003.
66. Alecci M and Jazzard P. Characterization and Reduction of Gradient-Induced Eddy Currents in the RF Shield of a TEM Resonator. *Magn. Reson. in Med.* 2002; **48**: 404-407.

67. Wadghiri YZ, Schneider A, Gray EN, Aristizabal O, Turnbull DH, Gutstein DE. High-Throughput  $\mu$ MRI Phenotyping of Right Ventricular Mouse Embryonic Abnormalities: Requirement for Intravascular Contrast Enhancement. Presentation # 18, at the 14<sup>th</sup> ISMRM. Seattle. 2006.
68. Hayes CE and Roemer PB. Noise Correlations in Data Simultaneously Acquired from Multiple Surface-Coil Arrays. *Magn. Reson. in Med.* 1990; **16**: 181-191.
69. Roemer PB, Edelstein WA, Hayes CE, Souza SP, Mueller OM. The NMR Phased Array. *Magn. Reson. Med.* 1990; **16**: 192-225.
70. Hardy CJ, Bottomley PA, Rohling KW, and Roemer PB. An NMR Phased Array for Human Cardiac <sup>31</sup>P Spectroscopy. *Magn. Reson. in Med.* 1992; **28**: 54-64.
71. Pruessmann KP, Weiger M, Scheidegger MB, and Boesiger P. SENSE: Sensitivity Encoding for Fast MRI. *MRM.* 1999; **42**: 952-962.
72. Reykowski A, Wright SM, Porter JR. Design of Matching Networks for Low Noise Pre-amplifiers. *Magn. Reson. in Med.* 1995; **33(6)**: 848-852.
73. Lanz T, Dodd S, Steinberger T, Silva A, Koretsky A. A 4-channel rat head array for 11.7T. Presented at *ESMRMB. Oral 81. Basle.* 2005.
74. Zhang X and Webb A. Design of a capacitively decoupled transmit/receive NMR phased array for high field microscopy at 14.1 T. *JMR.* 2004; **170**: 149-155.
75. Sutton BP, Ciobanu L, Zhang X and Webb A. Parallel Imaging for NMR Microscopy at 14.1 T. *MRM.* 2005; **54**: 9-13. <http://mrel.beckman.uiuc.edu/~lciobanu/pics/p9.pdf>
76. Dedeoglu A, Choi JK, Cormier K, Kowall NW, Jenkins BG. "MRS Analysis of Alzheimer's Disease Mouse Brain that Express Mutant Human APP Shows Altered Neurochemical Profile. *Brain Res.* 2004; **1012 (1-2)**: 60-5.
77. Wadghiri YZ, Sigurdsson EM, Sadowski M, Elliott JI, Li Y, Scholtzova H, Tang CY, Aguinaldo G, Pappolla M, Duff K, Wisniewski T, Turnbull DH. Detection of Alzheimer's Amyloid in Transgenic Mice Using MR Microimaging. *MRM.* 2003; **50**: 293-302.
78. Ohliger MA, Grant AK, and Sodickson DK. Ultimate Intrinsic Signal-to-Noise Ratio for Parallel MRI: Electromagnetic Field Considerations. *Magn. Reson. in Med.* 2003; **50**: 1018-1030.
79. Wiesinger F, Boesiger P, and Pruessmann KP. Electrodynamics and Ultimate SNR in Parallel MR Imaging. *Magn. Reson. in Med.* 2004; **52**: 376-399.
80. Lattanzi R, Grant AK, Ohliger MA, and Sodickson DK. Measuring Practical Coil Array Performance with Respect to Ultimate Intrinsic SNR: A Tool for Array Design and Assessment. Presentation # 424, at the 14<sup>th</sup> ISMRM. Seattle. 2006.
81. Yuan J, Wei J, Qu P and Shen GX. A Direct Modulated Optical Link for MR Coil Array Interconnect. Presented at the 14<sup>th</sup> ISMRM. Poster 2617. Seattle. 2006.
82. Oppelt R and Vester M. A low input impedance MRI preamplifier using a purely capacitive feedback network. Presented at the 14<sup>th</sup> ISMRM. Poster 2026. Seattle. 2006.
83. Sorgenfrei BL and Edelstein WA. Optimizing MRI SNR for Quadrature Unmatched RF Coils: Two Pre-amplifiers are Better Than One. *Magn. Reson. in Med.* 1996; **36**: 104-110.
84. Miller JB, Suits BH, Garroway AN, and Hepp MA. Interplay among Recovery Time, Signal, and Noise. *Concepts in Magn. Reson.* 2000; **12(3)**: 125-136.
85. Avago Technologies. ATF-58143 LN Enhancement Mode Pseudomorphic GaAs HEMT. 2004. <http://www.avagotech.com/pc/downloadDocument.do?id=4251> .
86. MR Product Information. Microwave Technology. Fremont CA. 2006. [www.mwtinc.com](http://www.mwtinc.com)
87. Kovacs H, Moskau D and Spraul M. Cryogenically cooled probes – a leap in NMR technology. *Mag. Reson. Spect.* 2005; **46**: 131-255.
88. Haueisen R, Marek D, Sacher M, Kong F, Ugurbil K and Junge S. Cryogenic Probe Setup for Routine MRI on Small Animals at 9.4 T. Presentation # 80, at *ESMRMB. Basle. Switzerland.* September 2005.
89. Hurlston SE, Brey WW, Suddarth SA, and Johnson GA. A High-Temperature Superconducting Helmholtz Probe for Microscopy at 9.4 T. *Magn. Reson. in Med.* 1999; **41**: 1032-1038.
90. Nouls J, Izenson M, Greeley H, Bagley M, Rozzi J and Johnson GA. A High-Temperature Superconducting Volume Coil for MR Microscopy at 9.4 T. Presented at 14<sup>th</sup> ISMRM. Poster #221. Seattle. 2006.
91. Darrasse L. and Ginefri J.-C. Perspectives with Cryogenic RF probes in biomedical MRI. *Biochimie.* 2003; **85**: 915-937.